ACS NANO

www.acsnano.org

ARTICLE

Kinetic Control of Angstrom-Scale Porosity in 2D Lattices for Direct Scalable Synthesis of Atomically Thin Proton Exchange Membranes

Nicole K. Moehring, Pavan Chaturvedi, Peifu Cheng, Wonhee Ko, An-Ping Li, Michael S. H. Boutilier, and Piran R. Kidambi*

Cite This: *ACS Nano* 2022, 16, 16003−16018

Read Online

ACCESS | Metrics & More | Article Recommendations | Supporting Information

ABSTRACT: **Angstrom-scale pores introduced into atomically thin 2D materials offer transformative advances for proton exchange membranes in several energy applications. Here, we show that facile kinetic control of scalable chemical vapor deposition (CVD) can allow for direct formation of angstrom-scale proton-selective pores in monolayer graphene with significant hindrance to even small, hydrated ions (K^+ diameter ∼6.6 Å) and gas molecules (H_2 kinetic diameter ∼2.9 Å). We demonstrate centimeter-scale Nafion|Graphene|Nafion membranes with proton conductance ∼3.3−3.8 S cm^{-2} (graphene ∼12.7−24.6 S cm^{-2}) and H^+/K^+ selectivity ∼6.2−44.2 with liquid electrolytes. The same membranes show proton conductance ∼4.6−4.8 S cm^{-2} (graphene ∼39.9−57.5 S cm^{-2}) and extremely low H_2 crossover ∼$1.7 \times 10^{-1} - 2.2 \times 10^{-1}$ mA cm^{-2} (∼0.4 V, ∼25 °C) with H_2 gas feed. We rationalize our findings via a resistance-based transport model and introduce a stacking approach that leverages combinatorial effects of interdefect distance and interlayer transport to allow for Nafion|Graphene|Graphene|Nafion membranes with H^+/K^+ selectivity ∼86.1 (at 1 M) and record low H_2 crossover current density ∼2.5×10^{-2} mA cm^{-2}, up to ∼90% lower than state-of-the-art ionomer Nafion membranes ∼2.7×10^{-1} mA cm^{-2} under identical conditions, while still maintaining proton conductance ∼4.2 S cm^{-2} (graphene stack ∼20.8 S cm^{-2}) comparable to that for Nafion of ∼5.2 S cm^{-2}. Our experimental insights enable functional atomically thin high flux proton exchange membranes with minimal crossover.**

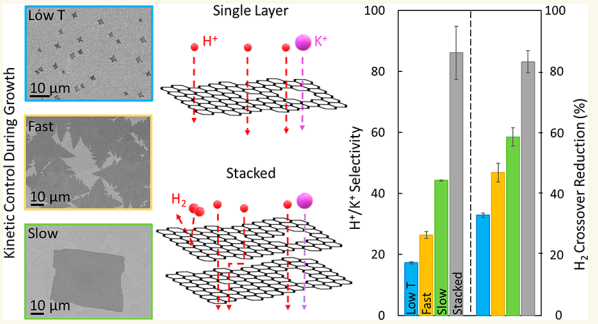

KEYWORDS: *graphene membranes, proton selectivity, hydrogen crossover, proton exchange membranes, Angstrom-scale pores, atomically thin membranes*

Selective and rapid transport of protons presents potential for transformative advances in several energy conversion/storage processes.[1] Proton exchange membranes (PEMs) in particular are expected to play a central role in enabling the hydrogen economy and climate change mitigation efforts by advancing applications such as fuel-cells,[2,3] redox-flow batteries,[4] and energy-efficient separations, for environmentally sustainable advances toward decarbonized/clean transportation, electricity grid storage technologies, distributed and mobile auxiliary power generation, among others.[1,5] Perfluorinated sulfonic-acid polymers, e.g., Nafion and sulfonated polyether ether ketone (SPEEK), currently represent the state-of-the-art conventional PEMs with proton conductance of ∼1−20 S cm^{-2} (depending on temperature and relative humidity),[2,6−8] but suffer from persistent issues of crossover (leakage of undesired species/reactants),[9,10] swelling, and softening at high relative humidity (>80%).[2,3,6] The hydration requirements for proton conductance in conventional PEMs further constrains operating temperatures,[2,5,6] limiting application potential and exacerbating efficiency losses over the application life-cycle.[1,5,10]

Here, proton permeation through the atomically thin lattice of 2D materials[11−13] such as graphene (∼3 mS cm^{-2}) and hexagonal boron nitride (h-BN, ∼100 mS cm^{-2}),[11] presents potential for transformative advances in PEMs.[1,14−18] The pristine graphene lattice represents an ideal PEM with a unique combination of atomic thinness,[1] proton permeation,[11,19−22] impermeability to small gases (e.g., He and larger mole-

Received: April 15, 2022
Accepted: September 15, 2022
Published: October 6, 2022

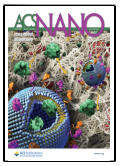

https://doi.org/10.1021/acsnano.2c03730
ACS Nano 2022, 16, 16003−16018

cules),[12,23] high mechanical strength (breaking strength ~42 N m^{-1}; withstands ~100 bar of applied pressure difference),[1,23,24] and chemical stability.[25,26] However, practical PEM applications with 2D materials will typically require (i) proton conductance >1 S cm^{-2} (significantly higher than pristine graphene ~3 mS cm^{-2});[1,11−13,20,21,27] as well as (ii) the development of scalable 2D material synthesis approaches (e.g., chemical vapor deposition (CVD));[28−34] and (iii) facile membrane fabrication processes,[32,34,35] e.g., by leveraging conventional PEM materials to support 2D materials and facilitate their device integration into applications.[1,14−18,36−41]

The introduction of nanoscale vacancy defects into the atomically thin lattice of 2D materials via approaches such as ion bombardment,[27,42] plasma treatments,[27,43,44] and oxidative etching[31,43,45−47] have been shown to significantly increase selective proton transport to ~0.01−4 S cm^{-2},[27,44] but the limited scalability of these methods, increased processing steps/costs, and challenges in achieving precise control over defect sizes in the sub-nanometer or angstrom scale hinders advances.[1] For example, Chaturvedi et al.[27] showed that defects created in the 2D lattice via ion bombardment (Ga^+ ion bombardment ~15 mS cm^{-2}, He^+ ion bombardment ~25 mS cm^{-2}), or plasma treatment (H_2 plasma ~40 mS cm^{-2}, N_2 plasma ~10 mS cm^{-2}) significantly increase proton conductance compared to as-synthesized CVD graphene ~4 mS cm^{-2}. Walker et al.[46] also reported an increase in proton conductance upon introduction of defects into the CVD graphene lattice via exposure to O_3 at 200 °C (current offset increased from ~0.03 to ~0.25 nA) while maintaining cation selectivity ~31−34 mV/log(M) (compared to an ideal membrane ~58 mV/log(M)). However, the selectivity decreased to ~14 mV/log(M) when larger defects ~1−6 nm were formed by further etching with $KMnO_4$ along with a 4× increase in membrane conductance.[46] While the presence of smaller defects can improve proton transport, large defects can compromise selectivity due to transport of undesired species,[25,26] i.e. hydrated ions with diameter ≥0.7 nm in redox flow batteries[4,48] or atoms/molecules (e.g., H_2 ~2.9 Å and O_2 ~3.5 Å kinetic diameters).[9,25]

In this context, scalable cost-effective synthesis of 2D materials via CVD[28−33,49,50] and related processes have typically focused on minimizing defects in the 2D lattice and/or minimizing grain boundaries by forming larger domains[1,33,51−53] to yield high-quality continuous monolayers for electronic applications. Some studies have explored the synthesis of nanoporous graphene for size-selective membrane applications by using lower CVD synthesis temperature,[32,34] pyrolyzing polymers/sugars on Ni substrate,[54] quenched hot Pt foils in hydrocarbons[55] to form nanoporous graphene,[22] synthesized monolayer amorphous carbon (MAC) via laser-assisted CVD,[56] introduced N dopants into graphene.[57] Notably, Griffin et al.[22] measured enhanced proton transport through micron-scale membranes of nanoporous graphene ~2 S cm^{-2} and MAC ~1 S cm^{-2} with H^+/Li^+ selectivity ~10 for both, while Zeng et al.[57] measured proton conductance of ~1.4 × 10^5 S m^{-2} (1 M HCl) for N-doped graphene (1 min N_2 plasma treatment of graphene) with H^+/Cl^- selectivity ~40 and H^+/methanol selectivity ~1−2 orders of magnitude higher than Nafion. Bukola et al.[38,39] reported proton conductance ~2−29 S cm^{-2} for CVD graphene (without any additional defect formation steps) and negligible transport of other cations while measuring two distinct centimeter-scale Nafion|Graphene|Nafion sandwich devices, i.e. one for proton transport and another for cation transport. Taken together, the introduction of angstrom-scale proton-selective defects into the lattice of 2D materials can potentially enhance proton permeation but the presence of even a small number of larger defects in the 2D lattice can adversely compromise membrane selectivity and performance. Facile and scalable processes to directly synthesize precise angstrom-scale pores over large-areas in 2D materials particularly for PEM applications remains elusive.

Here, we demonstrate that the growth kinetics of graphene CVD can be leveraged to introduce angstrom-scale proton-selective pores in the graphene for scalable, direct, and facile synthesis of large-area atomically thin high flux PEMs. Initially, we discuss facile kinetic control of scalable CVD process to introduce angstrom-scale pores in the graphene lattice for direct, bottom-up synthesis of PEMs before proceeding to study transport characteristics of H^+ using liquid electrolytes as well as H_2 gas as the proton source. We utilize conventional PEM polymers as supports to facilitate device integration of 2D materials and evaluate H^+ selectivity with respect to some of the smallest hydrated ions (K^+ and Cl^- ~6.6 Å) as well as the smallest energy relevant gas molecules (H_2 ~2.9 Å), with the rationale of higher or, at the very least, comparable selectivity for other larger ionic/molecular/gaseous species.[1,25]

RESULTS AND DISCUSSION

1. Kinetic Control of Graphene CVD for Introducing Angstrom-Scale Pores in the 2D Lattice. Initially, we leverage the kinetics of the CVD process, that is, nucleation followed by growth of nuclei, to modulate the rate of monolayer graphene synthesis on polycrystalline Cu foils[24,28,30−34,49,50] and introduce varying levels of defects (Figure 1). Specifically, we probe extremities of the kinetic regime of the graphene CVD process to synthesize three distinct kinds of monolayer graphene (see Experimental Methods, Figure 1A and Figure S1), namely, (i) slow growth−representing slower graphene growth kinetics achieved by using high H_2 gas flow into the CVD reactor which reduces the CH_4 partial pressure as well as etches defective clusters (carbon atoms attaching to the growing domain in configurations other than the perfect sp^2 bonded 2D lattice) attaching to the crystal edge during CVD, thereby slowing the growth rate and allowing for a lower density of defects in the synthesized graphene;[58,59] (ii) fast growth−representing faster graphene growth kinetics achieved by increasing the CH_4 precursor partial pressure by using lower H_2 gas flow into the CVD reactor as well as reduced etching of defective cluster attaching to the rapidly growing graphene crystal/nuclei edge during CVD;[58,59] and (iii) low-temperature growth[31,32] (Low T) − represents a combination of low CVD temperature (lower desorption kinetics) and lower H_2 gas flow into the CVD reactor that together allow for increased supersaturation of the catalyst surface resulting in higher nucleation density as well as rapid film growth by a higher propensity of defective cluster attachment at the edges and a significantly higher number of nuclei on the catalyst surface (Figure 1C).[32,60] Indeed, the nucleation density of the low T graphene ~8.9×10^3 mm^{-2}, is significantly higher than the fast (~1.4×10^3 mm^{-2}) and slow growth (~3.8×10^2 mm^{-2}) as shown in Figure 1C.[61−63]

The influence of the kinetic extremities in graphene CVD processes can be observed via the graphene nucleation density (Figure 1C) as well as the graphene coverage on the Cu

https://doi.org/10.1021/acsnano.2c03730
ACS Nano 2022, 16, 16003−16018

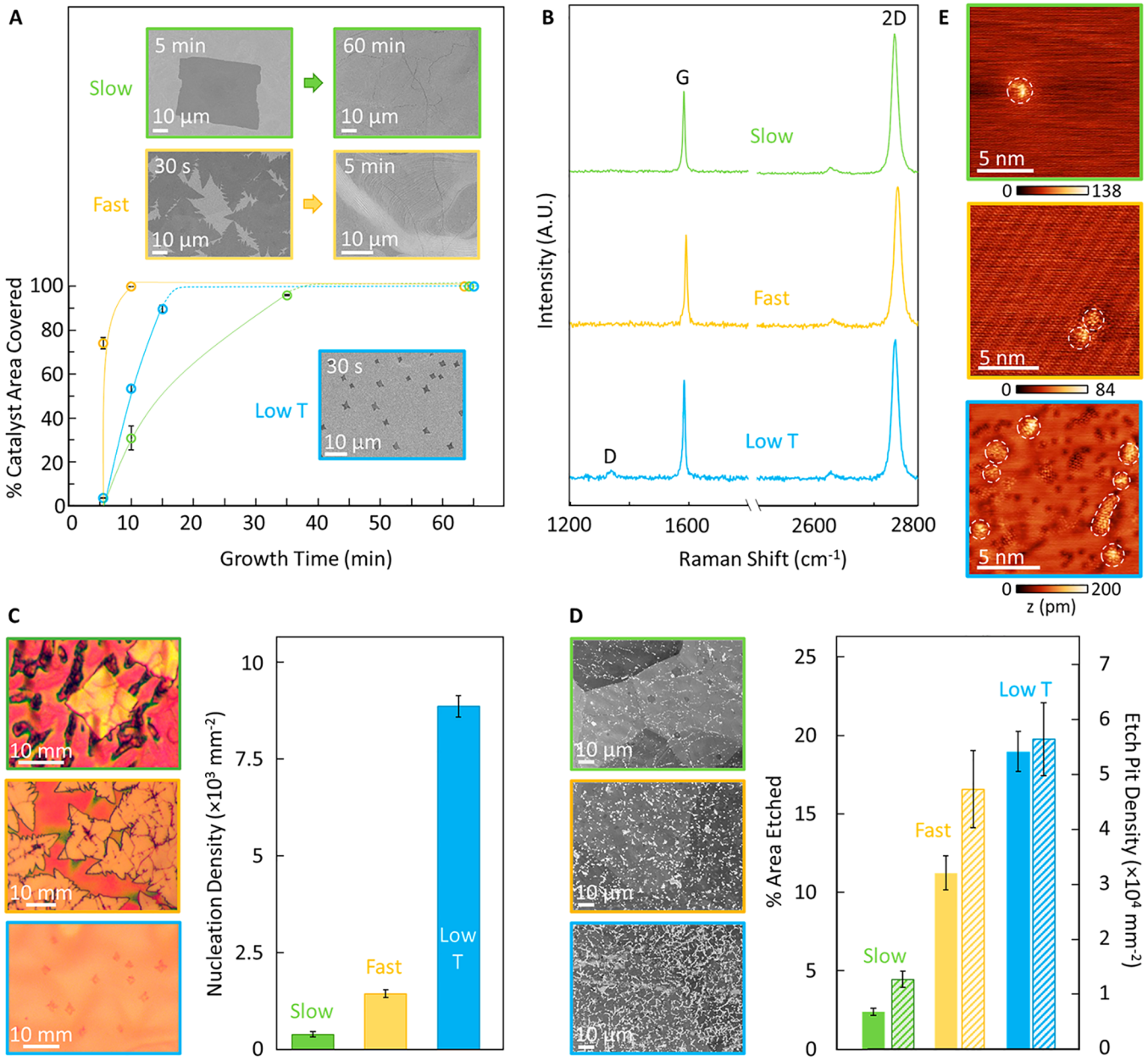

Figure 1. Kinetic control of graphene CVD for angstrom-scale proton-selective nanopores. (A) Graphene coverage of Cu catalyst foil as a function of time for slow (green), fast (yellow) and low T (blue) graphene representing extremities of the kinetic regime for CVD growth. Note the dotted lines are just a guide for the eye. Inset SEM images show differences in graphene domain shape as well as time required for attaining continuous films (identified via the presence of wrinkles in SEM images). (B) Raman spectra for slow, fast, and low T graphene after transfer to 300 nm SiO_2/Si wafer. Only the low T graphene shows a noticeable D peak at ~1350 cm^{-1}. (C) Optical images of graphene domains on Cu after heating in air at 220 °C for ~15 min shows oxidation of Cu in regions not covered by graphene for slow (~2 min growth time), fast (~30 s growth time), and low T (~30 s growth time). The fast graphene shows oxidation in the center of the domain (darker contrast in optical images) extending into each of the 4 lobes while the slow growth does not. Nucleation density for slow (~2 min growth time), fast (~30 s growth time), and low T (~30 s growth time) growth is obtained by processing optical (panel C) and SEM images (also see Figure S3) of graphene domains on Cu foil. (D) Representative SEM images for fast, slow and low T growth graphene on Cu foil after electrochemical etch test (0.5 M $CuSO_4$ solution at 1 V for 1 s) as well as percentage area etched (solid bar, left side *Y*-axis) and etch pit density (striped bar, right side *Y*-axis). Bright spots in the SEM images represent etch pits in the Cu formed underneath defects in the continuous monolayer graphene film. The slow growth graphene has the lowest density of etch pits, followed by the fast growth that shows a significant increase while the low T graphene has the highest density of etch pits. Darker regions in the top SEM image (green, slow) correspond to different grains in the polycrystalline Cu foil. All error bars in Figure 1 represent one standard deviation. (E) STM images of nanopores (circled in white) within the lattice of slow (green), fast (yellow), and low T (blue) graphene, with respective *z*-scale bars below in pm. Imaging bias V = 0.1 V for all images and set point current I = 1 nA for slow and fast graphene, and I = 0.5 nA for low T graphene. The additional periodic line-like pattern observed for the fast graphene STM image is a Moire pattern between Cu and the graphene lattice.

catalyst as a function of time and the shape of the graphene domains (Figure 1A), while defect densities can be evaluated via Raman spectroscopy (Figure 1B), electrochemical etch tests (Figure 1D), and acid etch tests (Figure S2). An analysis

https://doi.org/10.1021/acsnano.2c03730
ACS Nano 2022, 16, 16003−16018

of SEM images of graphene coverage on Cu (Figure 1A, Figure S3) after ~5 min of growth shows ~30% (slow), ~100% (fast), and ~53% (low T) coverage, while complete monolayer films are obtained after >45 min (slow), ~5 min (fast), and >15 min (lines are a guide for the eye). The differences in graphene growth rates are attributed to differences in H_2 partial pressure and corresponding etching rates as well as differences in nucleation densities (Figure 1C). Lower H_2 partial pressures typically resulted in faster graphene growth,[59] as seen from the measured pressure ~12−13 Torr (slow), ~1−2 Torr (fast), ~1−2 Torr (low T) during CVD. We note that the nucleation, etching, and/or the formation rates at lower temperatures[32,59,60,63,64] can also be distinctly different than higher temperatures (due to lower precursor dissociation, lower mobility of clusters, etc.), resulting in the growth rate for the low T graphene being slower than the fast growth graphene.[61,62] We emphasize that whether H_2 or impurities in H_2 etches graphene on Cu remains unresolved in the literature,[65] but for the purposes of our study, we used H_2 gas (99.999% purity) from the same gas cylinder for all experiments to ensure consistency in the experiments.

In addition to differences in the growth rates, the graphene domain shapes also provide insights into the growth kinetics (Figure 1A,C). The slow growth domains have smooth edges indicative of enhanced etching at the graphene domain edges,[59,64,66] while the fast growth graphene shows four-lobed graphene domains with dendritic edges due to the lower etching as well as faster attachment/propagation of adatom clusters along the crystallographic directions of the lobes.[67,68]

Oxidation of the graphene domains on Cu serves as a qualitative indicator of differences in graphene quality since the oxidation of the Cu is only expected to occur underneath regions not covered by graphene (i.e., underneath defects in graphene).[69] The fast growth graphene shows oxidation in the center of the domain which then expands outward in the direction of the domain lobes (Figure 1C, optical images). Such oxidation is not observed on the slow growth domains indicating higher quality within the domains. Raman spectra of the synthesized CVD graphene (Figure 1B) confirms monolayer films (2D ~2700 cm^{-1}, G ~1600 cm^{-1} and D ~1350 cm^{-1} and I_{2D}/I_G >1). Only the low T graphene showed a noticeable D peak indicative of defects and is consistent with our own prior work.[31,32] Quantitative analysis (I_D/I_G) shows the defect density of ~0.02 (slow) < ~0.04 (fast) < ~0.08 (low T), wherein the slow growth graphene showed the highest quality.[31,32,34,70] However, Raman spectroscopy is limited to the spot size of the incident laser (~1 μm) and mapping centimeter-scale areas relevant for PEM and membrane applications is impractical.

Hence, we performed electrochemical etch test (see Experimental Methods and Figure 1D) and acid etch test (Figure S2) to form etch pits in Cu underneath defects in graphene to obtain insights on graphene quality and defects density over large areas relevant for PEM and membrane applications. Etch pits in Cu occurs where graphene defects are ~0.6−0.7 nm in size or larger (limited to the size of the hydrated Cu^{2+} ions which must leave the Cu surface through the defects)[30] and the resulting etch pits appear as bright spots when characterized using SEM (Figure 1D). Assuming each bright spot corresponds to an etch pit that originated from a defect, we calculate a defect density (see Experimental Methods and Figure 1D) of ~1.3×10^4 mm^{-2} (slow growth, total etched area ~3.2%), ~4.7×10^4 mm^{-2} (fast growth, total etched area ~11.2%), and ~5.6×10^4 mm^{-2} (low T, total etched area ~18.9%). Notably the defect density for our fast growth graphene is found to be in agreement with our own prior work with CVD graphene (~3.36×10^4 mm^{-2}) for centimeter-scale atomically thin membranes.[30,39] A similar trend for defect density i.e. slow < fast < low T is also seen for acid etch test[30] using 0.1 M $FeCl_3$ solution (Figure S2). Finally, scanning tunnelling microscopy (STM) is used to directly image and confirm the presence of defects within the lattice of slow, fast, and low T graphene (Figure 1E) that manifest as nanopores in an atomically thin membrane. We note that the defects appear bright due to the increased local density of states by defect sites.[71] Having characterized the defect density qualitatively and quantitatively for each graphene type, we proceed to investigate transport.

2. Diffusion-Driven Ionic and Molecular Transport through Atomically Thin Graphene Membranes. We utilize diffusion-driven ionic and molecular transport to obtain insights on the presence of sub-nanometer scale or angstrom-scale defects (Figure 2) over centimeter scale areas in each of

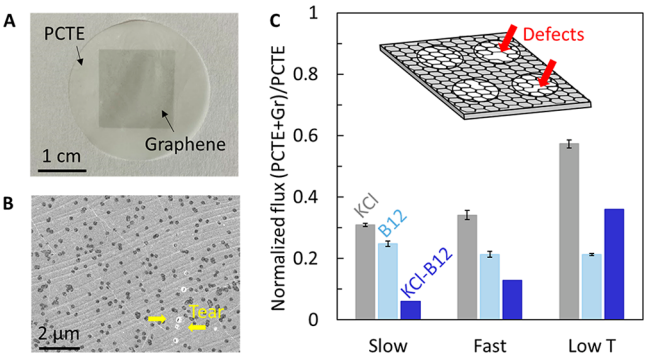

Figure 2. Diffusion-driven transport through angstrom and nanoscale defects in graphene that manifest as nanopores in an atomically thin membrane. (A) Optical image of centimeter-scale graphene transferred to polycarbonate track etched (PCTE) supports with ~200 nm pores. Typical transfer yields are >95% (see Figure S4).[34] (B) SEM image of graphene on PCTE shows the majority of PCTE pores are covered by graphene (darker contrast). Tears in the graphene (yellow arrows) result in the uncovered PCTE regions which appear brighter due to polymer charging during SEM imaging. (C) Normalized diffusive flux for graphene membranes (PCTE+G)/PCTE for KCl (~0.66 nm, gray) and Vitamin B12 (~1−1.5 nm, light blue).[34] Differences in normalized flux of KCl and B12 (dark blue bar) indicates the presence of intrinsic subnanometer defects ~0.66−1.5 nm in graphene. We observe the fewest sub-nanometer defects in slow graphene, followed by the fast and then the low T growth graphene. Error bars indicate one standard deviation.

the synthesized CVD graphene representing the extremes of the kinetic regime. The synthesized graphene is transferred on to polycarbonate track-etched (PCTE) support with well-defined cylindrical ~200 nm pores[30−34] and diffusion-driven transport of different species (KCl ~0.66 nm, and Vitamin B-12 ~1−1.5 nm) is measured (see Experimental Methods, Figure 2A). The graphene transfer process can introduce some macroscopic tears (SEM image in Figure 2B). We initially quantify such large tears in graphene using pressure-driven-ethanol transport, that is, tear/defect >50 nm will present similar resistance to ethanol transport as that of a bare PCTE support pore ~200 nm (see Experimental Methods and Figure S4).[28,30,31] Having confirmed <5% of tears (graphene coverage

https://doi.org/10.1021/acsnano.2c03730
ACS Nano 2022, 16, 16003−16018

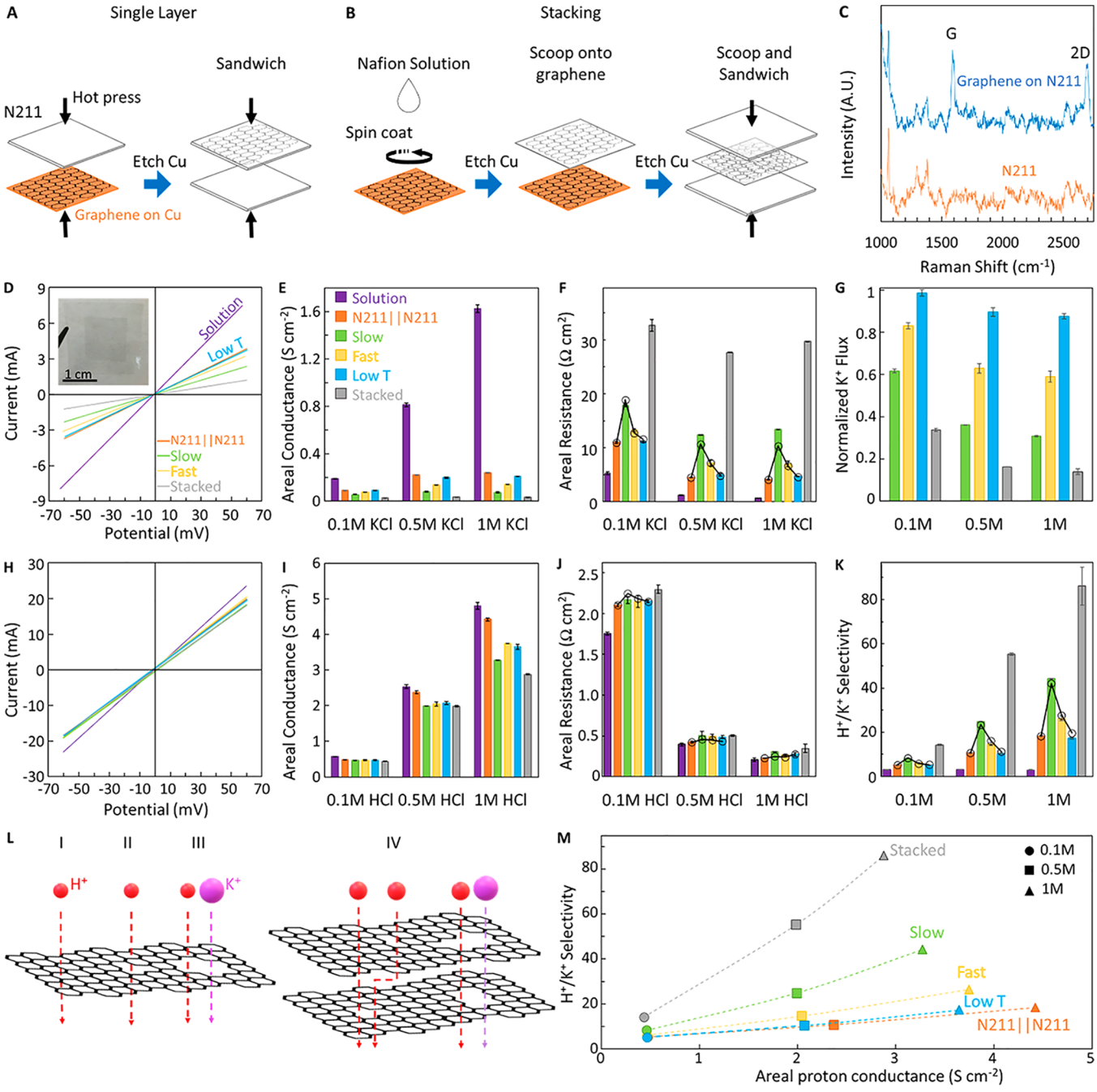

Figure 3. Liquid phase ionic transport through centimeter-scale graphene membranes. Schematic of the fabrication process for centimeter-scale (A) N211|Graphene|N211 membranes via hot pressing and (B) N211|Graphene|Graphene|N211 membranes via stacking. Inset of panel D shows an optical image of the N211|Graphene|N211 membrane (also see Figure S5). (C) Raman spectroscopy confirms successful graphene transfer to Nafion 211 via the presence of the characteristic G and 2D peaks. *I*−*V* curves extracted from chronoamperometry measurements (see Experimental Methods and Figure S6) for slow (green), fast (yellow) and low T (blue) growth graphene sandwich membranes measured in (D) 0.1 M KCl and H) 0.1 M HCl, respectively. Note, the 0.1 M KCl measurements were performed using Nafion converted to K^+ form and subsequently converted to H^+ form for measurements in 0.1 M HCl (see Experimental Methods). Also shown is 2 layers of slow growth graphene (stacked, gray) sandwiched between Nafion 211. Areal conductance (calculated from the slope of the I−V curves and dividing by the active area ~0.68 cm^2) measured using 0.1M, 0.5M, and 1 M of (E) KCl and (I) HCl, respectively. Membrane areal resistances (calculated by taking the inverse of the areal conductance in (E) and (I) for 0.1 M, 0.5 M, and 1 M of (F) KCl and (J) HCl, respectively. (G) Normalized K^+ flux is used to evaluate the reduction in K^+ conductance upon the addition of graphene as compared to a bare Nafion 211 sandwich control membrane and serves as a measure of graphene coverage as well as nanoscale defects that allow K^+ transport. (K) H^+/K^+ selectivity for the fabricated membranes with different electrolyte concentrations. Circles on the bar plots in panels F,J,K represent calculated values from resistance based transport model and show good agreement with experimental measurements. Error bars represent one standard deviation. (L) Schematic illustrating graphene H^+/K^+ selectivity in the absence and presence of defects. Arrows indicate potential transport paths for H^+ (red) and K^+ (purple). The pristine graphene lattice can allow for H^+ transport (I), defects smaller <0.66 nm will allow for enhanced H^+ transport but hinder K^+ transport (II, selective transport), and defects >0.66 nm will allow both H^+ and K^+ transport (III, nonselective transport). Schematic of two layers of graphene stacked on top of each other illustrating interlayer transport

https://doi.org/10.1021/acsnano.2c03730
ACS Nano 2022, 16, 16003−16018

Figure 3. continued

in addition to transport through one layer (IV). H^+ transports through the pristine lattice as well as small and large defects, while K^+ transport remains limited to defects >0.66 nm (hydrated K^+ diameter). M) H^+/K^+ selectivity for graphene membranes plotted as a function of liquid-phase proton conductance, demonstrating the improvement in selectivity with minimal decrease in areal proton conductance via facile stacking of slow growth graphene.

on PCTE >95%) for the slow, fast, and low T graphene (Figure S4), we proceed to probe diffusion-driven transport using aqueous solutions of KCl and B12.[31,34]

A comparison of the normalized flux (transport through the graphene+PCTE/transport through bare PCTE support) shows normalized KCl flux ∼30.8% (slow growth), ∼34.1% (fast growth), and ∼57.3% (low T) graphene (Figure 2C), indicating the low T graphene has the largest fraction of defects >0.66 nm.[31−34] The normalized B12 flux are ∼24.7% (slow growth), ∼21.3% (fast growth), and ∼21.2% (low T) graphene (Figure 2C).[32] The difference between the normalized flux of KCl and B12 for each CVD graphene provide insights on the presence of defects between ∼0.66 to 1−1.5 nm, and this difference is lowest for slow growth graphene (∼6.1%), followed by fast growth (∼12.8%), and then low T growth (∼36.1%). These observations suggest the slow growth graphene has the fewest number of defects between 0.66 to 1−1.5 nm, while the low T graphene has the most and is fully consistent with the insights on graphene quality via qualitative and quantitative analysis in Figure 1, indicating facile kinetic control of the CVD process can indeed allow for the introduction of varying levels of angstrom-scale pores in the graphene lattice. Notably, increased KCl leakage with increasing defect density suggest a relatively uniform distribution of defects within the graphene lattice (considering a uniform PCTE porosity ∼10%, PCTE pore diameter ∼200 nm, and graphene domain sizes in the micron scale, the propensity of grain boundary overlap is minimal), representing an advantage over engineering grain boundaries[72] and is further corroborated via STM images and etch test images in Figures 1 and S2 that show nanopores within a graphene domain.

3. Liquid-Phase Electrically Driven Transport through Centimeter-Scale Nafion|Graphene|Nafion Membranes. To investigate the role of angstrom-scale defects on H^+ transport and cation selectivity, we incorporate the graphene in PEMs and measure electrically driven transport through each of the synthesized CVD graphene in liquid electrolytes. The rationale for sandwiching graphene in between Nafion was to facilitate facile device integration as well as to prevent physical damage to the graphene via abrasion while mounting the PEMs into the experimental setup. The use of Nafion also serves as effective controls/references to deconvolute transport characteristics of the embedded monolayer CVD graphene.

Centimeter-scale graphene-based PEMs were fabricated from each of the synthesized CVD graphene by sandwiching them between Nafion 211 (N211, ∼20 μm thickness) via hot-press followed by etching of the Cu foil (see Experimental Methods)[38,39] and electrically driven transport of K^+ and H^+ was measured using liquid electrolytes (Figure 3). Additionally, we also introduce a facile method for stacking two graphene layers via spin coating a thin layer of Nafion and using it to transfer one layer of graphene on to another (see Experimental Methods and Figure 3B). Both methods (Figure 3A,B) allow for direct transfer of CVD graphene to N211 without potential influence of contamination from sacrificial polymer transfer processes.[35] Successful large-area graphene transfer is confirmed via optical images that show a region of darker contrast compared to Nafion (see inset in Figure 3D) and graphene characteristic features such as wrinkles observed in SEM images of graphene transferred to Nafion (Figure S5). Raman spectroscopy also confirms graphene transfer to N211 with the characteristic 2D and G peaks for graphene (Figure 3C). However, the Raman spectrum for Nafion has several peaks in the region between 1100−1500 cm^{-1} that overlap the region for the graphene D-peak (∼1350 cm^{-1}) and make I_D/I_G analysis after transfer nontrivial.

Having confirmed graphene transfer to N211 and successful fabrication of centimeter-scale graphene- based PEMs, we proceed to measure liquid-phase electrically driven ion transport through the PEMs in a custom-built H-cell (see Experimental Methods and Figure S6). The rationale for measuring transport in KCl in addition to HCl is (i) the common anion Cl^-, (ii) K^+ and Cl^- represents one of the smallest hydrated ions ∼0.66 nm in diameter, and (iii) to allow for a comparison with the diffusion-driven flow experiments using KCl in Figure 2C. Current (I) is measured via multiple step chronoamperometry (see Experimental Methods and Figure S6B) and the current at each potential (V) is used to obtain $I-V$ curves for each PEM for both KCl (Figure 3D) and HCl (Figure 3H). Measuring K^+ and H^+ on the same membrane allows effective assessment of the influence of subnanometer scale defects in graphene on PEM characteristics i.e. H^+ conductivity and H^+/K^+ selectivity.

The PEM conductance is calculated from the slope of the $I-V$ curves in Figure 3D,H and normalized by dividing by the active area (∼0.68 cm^2) to yield areal conductance for KCl (Figure 3E) and HCl (Figure 3I). The inverse of areal conductance (i.e., areal resistance) is used to isolate the contribution of the different CVD graphene types from the Nafion sandwich device via a series resistance analysis for KCl (Figure 3F) and HCl (Figure 3J). For each PEM, KCl transport was first measured with increasing electrolyte concentration (0.1−1 M, Figure 3E,F) since the Nafion was pre-exchanged to K^+-form (see Experimental Methods) and subsequently an H^+-form exchange was performed (see Experimental Methods and Figure S7) before measuring in increasing concentrations of HCl (Figure 3I,J). We emphasize that our approach effectively minimizes influence/variations from graphene transfer yield and membrane to membrane variation allowing for a clear interpretation of the influence of defects on transport. Complete exchange of the Nafion from acid form (as received) to K^+ salt form and vice versa was ensured to avoid contributions from mixed currents from H^+ and K^+ (see Experimental Methods and Figure S7).

Notably, the PEM membranes with slow growth graphene demonstrates the highest areal resistance to K^+ transport (∼17.8 Ω cm^2 with 0.1 M KCl, Figure 3F) consistent with the lowest defect density (Figure 1 and Figure 2), followed by the fast growth (∼13.2 Ω cm^2 with 0.1 M KCl) while the low T graphene (∼11.1 Ω cm^2 with 0.1 M KCl) shows a marginal increase in areal resistance to K^+ transport compared to the

https://doi.org/10.1021/acsnano.2c03730
ACS Nano 2022, 16, 16003−16018

Nafion sandwich control (~11.0 Ω cm^2) indicating a large number of defects >0.66 nm and is fully consistent with the diffusion-driven transport of KCl (Figure 2) and defect density (Figure 1). A similar trend is seen with increasing KCl concentrations to 0.5 and 1 M (Figure 3D, Table S1, Table S2), although the absolute values of resistance are lower. We propose our observations at higher salt concentrations could arise from a combinatorial interplay of (i) lower solution resistance at higher concentrations,[73] (ii) membrane hydration,[74−76] and (iii) Donnan exclusion effects.[74,75,77] For example, at higher KCl concentrations, the solution resistance is not only lower but additionally, the Nafion channel characteristics can change and ion partitioning within the channels could occur, with higher concentrations of salt solution leading to channel dehydration and changes to porosity.[74,76,77] Further, the concentration of co-ions within the membrane can also reduce the effect of the negatively charged sulfonated groups, resulting in additional permeation of counterions via Donnan exclusion.[74,76,77] Regardless of the absolute resistance values at higher KCl concentrations (0.5 and 1 M), we note the trend in resistance holds i.e. resistance to K^+ transport of slow growth graphene > fast growth graphene > low T graphene > Nafion control (Figure 3D and Table S1).

Assuming a series resistance model, the measured areal resistance is the sum of the individual resistances i.e. R_{total} = system (R_{system}) + solution ($R_{solution}$) + Nafion (R_{Nafion}) + graphene ($R_{graphene}$), allowing for the isolation of the resistance contribution from the graphene alone by subtracting the other components (see Table S1).[39] Such an analysis yields K^+ areal resistance values at 0.1 M KCl of ~6.8 Ω cm^2 (slow growth), ~2.2 Ω cm^2 (fast growth), and ~1.5 × 10^{-1} Ω cm^2 (low T) (Table S1) or areal conductance ~1.5 × 10^{-1} S cm^{-2} (slow growth), ~4.5 × 10^{-1} S cm^{-2} (fast growth) and ~6.6 S cm^{-2} (low T) (Table S2). The normalized K^+ flux (conductance of Nafion|Graphene|Nafion/Nafion||Nafion controls, Figure 3G) shows the addition of slow growth graphene reults in the lowest K^+ flux (~6.2 × 10^{-1} at 0.1 M) as compared to the control membrane, indicating it has the lowest density of defects >0.66 nm, followed by fast growth graphene (~8.3 × 10^{-1}) and low T graphene (~9.8 × 10^{-1}) and a similar trend is also seen at 0.5 and 1 M KCl.

After measuring K^+ transport, the same membranes are converted into acid (H^+) form and measured in 0.1−1 M HCl (Figure 3H-J) and analyzed via the resistance model (Table S1). We emphasize that measuring K^+ transport and using the exact same membrane for H^+ transport allows for a direct comparison between defect density and H^+ transport rate as well as an accurate measure of H^+/K^+ selectivity. The measured areal proton conductance at 0.1 M HCl ~4.6 × 10^{-1} S cm^{-2} (slow growth), ~4.7 × 10^{-1} S cm^{-2} (fast growth) and ~4.7 × 10^{-1} S cm^{-2} (low T graphene), while the Nafion sandwich control is ~4.8 × 10^{-1} S cm^{-2} (also see Tables S1 and S2 for 0.5 and 1 M), suggesting rapid H^+ transport through defects which allowed K^+ transport as well as other smaller defects and through the pristine lattice. Isolating the areal proton conductance of graphene by subtracting the resistance contribution from the solution and Nafion yields ~16.1 S cm^{-2} (slow growth), ~ 23.4 S cm^{-2} (fast growth), and ~22.0 S cm^{-2} (low T graphene) with 0.1 M HCl. The ratio of H^+ areal conductance to K^+ areal conductance provides H^+/K^+ selectivity (Figure 3K and Table S3). The selectivity of slow growth > fast growth > low T graphene for all electrolyte concentrations, and the selectivity increases with increasing electrolyte concentration from 0.1 to 1 M.

To further increase H^+/K^+ selectivity without adversely affecting H^+ conductance, we developed a graphene stacking approach (Figure 3B) that allows for sealing of nonselective defects in one layer by the second layer,[78] while still allowing for proton transport to occur via defects in both layers as well as the interlayer spacing.[78−83] Hence, the defect density in the graphene layers and the inter-defect distance emerge as important parameters. We specifically select the slow growth graphene due to its lower density of defects while still exhibiting high H^+ conductance and stack two layers of the slow growth graphene, embed them into a Nafion sandwich and evaluate liquid phase transport. Notably, we observe a significant resistance to K^+ transport (~32.6 Ω cm^2 at 0.1 M KCl, also see Table S1 and S2) but H^+ resistance only increases marginally (~2.3 Ω cm^2 at 0.1 M HCl) with the addition of the second layer (Figure 3F,J, gray bar) when compared to only 1 layer of the slow growth graphene (~2.1 Ω cm^2 at 0.1 M HCl). We hypothesize this effect originates from (i) the higher interlayer transport of H^+ compared to K^+,[82,83] as well as (ii) the low number of defects large enough for K^+ to transport through upon stacking two layers of slow growth graphene, as K^+ will only transport through overlapping defects >0.66 nm in diameter (Figure 3L,M).[78] This increase in K^+ resistance but low H^+ resistance is seen in the high H^+/K^+ selectivity ~55.4 at 0.5 M and up to ~86.1 at 1 M for the stacked slow graphene (Figure 3M). Taken together, the combination of a low density of defects in slow growth graphene, sealing nonselective defects by stacking another layer and rapid interlayer proton transport between the stacked layers allow for enhanced H^+/K^+ selectivity without a significant loss in H^+ conductance compared to the Nafion sandwich control membranes.

4. Modeling Liquid-Phase H^+ and K^+ Transport through Nafion|Graphene|Nafion Membranes. We employ a simple transport model to further understand the measured H^+ and K^+ resistances. The measured transport of K^+ as well as the higher transport rates for H^+ (compared to the pristine graphene ~3 mS cm^{-2}) is attributed to pores in the graphene. Previous reports have divided these pores by size into larger tears (>50 nm) and smaller defects,[78] both of which can conduct ions (Figure 4). To cross the graphene membrane, ions pass through the Nafion support, then through either tears or defects, and finally through the second layer of Nafion, as illustrated by the equivalent resistance network in Figure 4A. The total resistance to passing through a membrane consisting of a single layer of graphene between two Nafion layers is then

$$R_{1-layer} = 2R_{nafion} + \left(\frac{a}{R_{tears}} + \frac{1-a}{R_{defects}}\right)^{-1} \quad (1)$$

where R_{nafion}, $R_{defects}$, and R_{tears} are the resistances to passing through a single Nafion layer, defects in the graphene, and tears in the graphene, respectively, and a is the fraction of membrane area occupied by tears.

The measured resistance through Nafion for each concentration was used directly in the model. The resistances through single tears and defects were modeled as continuum transport with the access resistance to reaching the pore in series with the resistance to passing through the pore[84]

https://doi.org/10.1021/acsnano.2c03730
ACS Nano 2022, 16, 16003−16018

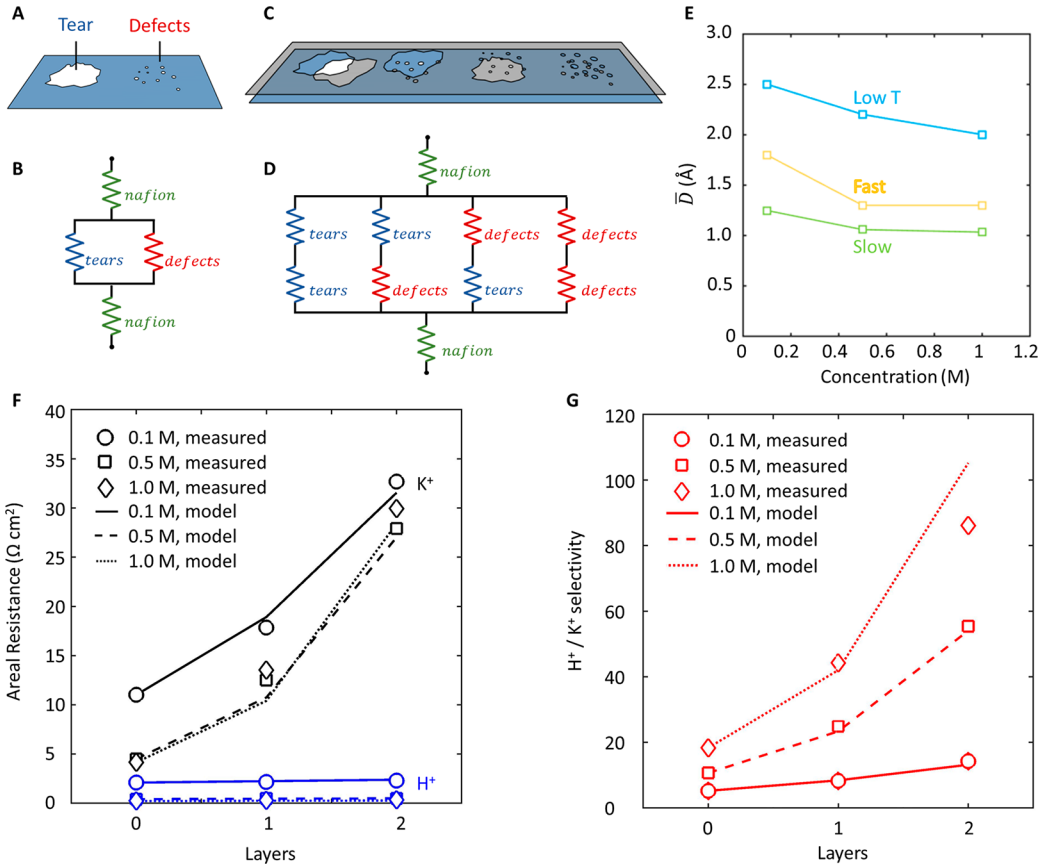

Figure 4. Resistance model for ion transport. (A) Schematic of defects and tears in atomically thin graphene membranes and (B) equivalent resistance network. (C) Schematic of defects and tears and (D) equivalent resistance network for two layers of graphene stacked. (E) Pore size distribution parameter, $\bar{D}$, used in model and its variation with concentration. Comparison of (F) measured areal resistance and (G) selectivity for graphene (slow growth) with the model shows very good agreement. The measured values plotted are the average values for the N211||N211, slow, and stacked membranes at each concentration from Figure 3J and 3K, respectively.

$$R_D = \frac{4t}{\pi\sigma(D - D_{ion})^2} + \frac{1}{\sigma(D - D_{ion})} \quad (2)$$

Here, σ is the conductivity of the solution, D is the pore diameter, t is the pore thickness, and D_{ion} is the effective ion diameter (taken as the hydrated diameter of ~0.66 nm for K^+, and 0 for H^+ since it can even pass through pristine graphene).

Tear sizes vary depending on the conditions of processing to fabricate the membranes and their distribution is not exactly known. We approximate tears as all having the same diameter, D_{tear}, and producing an open area fraction of a. Tears are much larger than the ion diameter and membrane thickness, reducing eq 2 to

$$R_{tears}A = \frac{\pi D_{tear}}{4\sigma} \quad (3)$$

where A is the membrane area. The defect size in graphene commonly follows an approximately exponential distribution of the form[85]

$$p(D) = \frac{1}{\bar{D}} e^{-D/\bar{D}} \quad (4)$$

where $p(D)$ is the probability density that a defect has diameter D and the parameter $\bar{D}$ determines the width of the distribution. Summing the resistance through each defect in parallel, the average overall membrane resistance due to defects becomes,

$$(R_{defects}A)^{-1} = \int_{D_{ion}}^{\infty} \frac{n\sigma}{\frac{4t}{\pi(D - D_{ion})^2} + \frac{1}{D - D_{ion}}} p(D)dD \quad (5)$$

where n is the defect density (number of defects per unit area).

Although the model has several parameters that are unknown, prior studies provide an approximate range for these values. Here we select reasonable values for the various parameters to show that the measured resistances can be explained by the proposed transport pathways. We model tears as having diameter D_{tear} = 200 nm and covering 0.1% of the membrane area. Both the defect density and number of defects could differ between graphene prepared by the slow, fast, and low temperature recipes. However, the H^+ resistance is similar for all three (Figure 3J, open circles) even though the K^+ resistance varies (Figure 3F, open circles). We therefore expect a greater difference in $\bar{D}$ than n between the different types of graphene. To reduce the number of parameters being varied, we select $n = 1.1 \times 10^{12}$ cm^{-2} and then adjust $\bar{D}$ for the different conditions. We note that this value of n is a similar defect density used in prior reports[31] and is greater than the defect density we obtained with the electrochemical etch test due to limitations on resolution in the defect size (>0.6–0.7 nm) it can probe.

The resulting model values are compared to experimental measurements in Figure 4F,G, and Figure 3F,J,K using the $\bar{D}$ values plotted in Figure 4E. The slow growth graphene

https://doi.org/10.1021/acsnano.2c03730
ACS Nano 2022, 16, 16003–16018

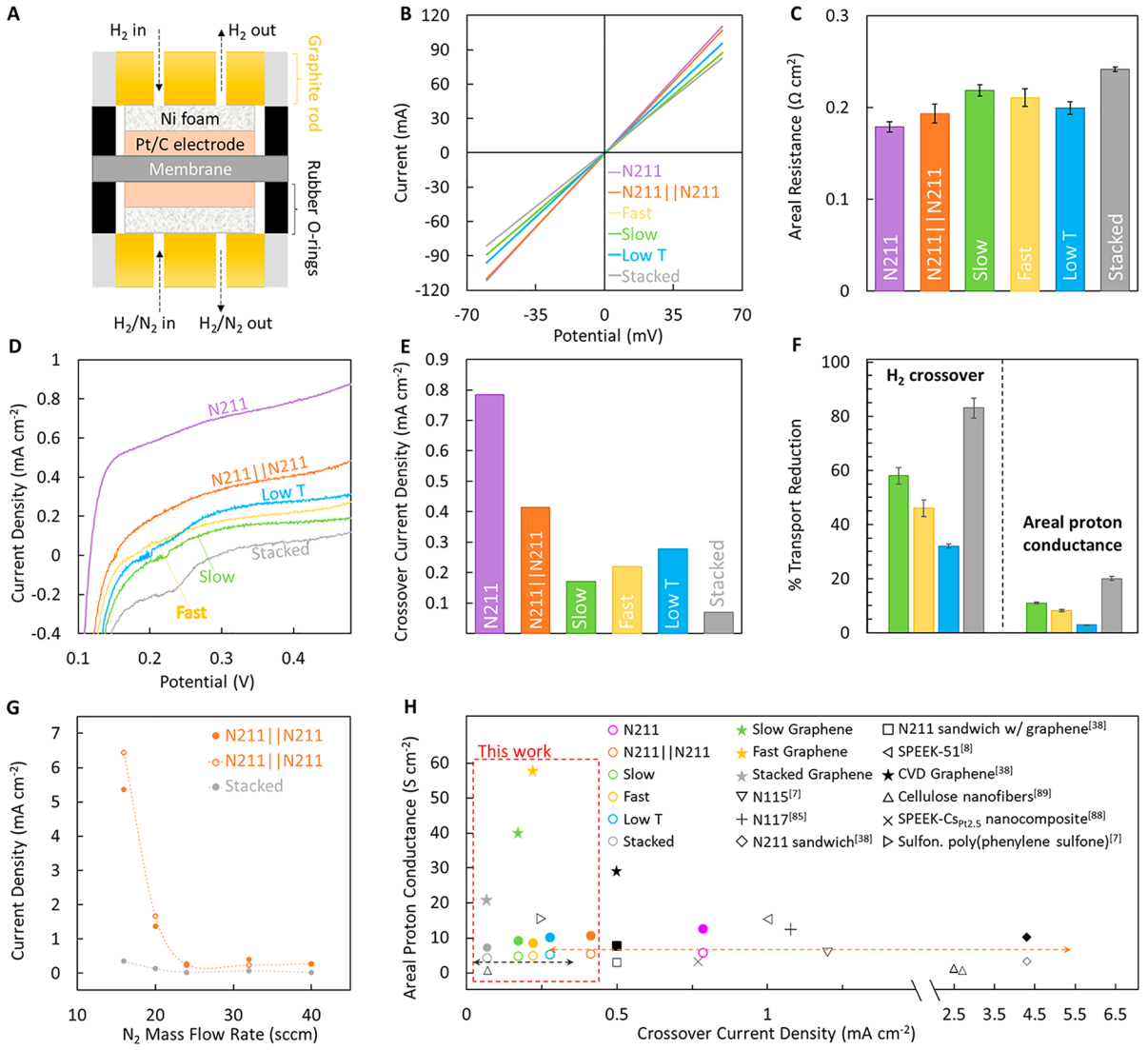

Figure 5. Gas phase H^+ and H_2 crossover through centimeter-scale graphene membranes. (A) Schematic of the setup used for measuring H^+ transport and H_2 crossover through N211|Graphene|N211 sandwich membranes with Pt/C cloth electrodes.[38] (B) I–V curves for slow, fast, low T, and stacked CVD graphene sandwiched between in N211 as well as N211 sandwich (control, N211||N211) measured by supplying H_2 gas to both sides of the membranes (symmetric mode, see Experimental Methods). (C) Computed areal resistance to proton transport for each membrane measured in B. (D) Crossover of H_2 measured via linear sweep voltammetry (LSV) while supplying 40 sccm H_2 to one side and ~32 sccm N_2 to the other side of the membranes (asymmetric mode, see Experimental Methods). The limiting current region between 0.1 and 0.5 V illustrates differences in H_2 crossover between membranes. Higher current densities indicate more H_2 crossover since proton current will only occur when H_2 gas crosses through the membrane to dissociate at the Pt electrodes on the N_2 side. (E) Crossover current density at 0.4 V and 25 °C from D is used to compare H_2 crossover across the different membranes.[10,17] (F) Reduction in H_2 crossover compared with the reduction in H^+ transport through the membranes, calculated from the average H_2 crossover and H^+ transport values for each graphene membrane compared to the average of the N211||N211 sandwich. The slow growth graphene allows for ~58% (~1.7×10^{-1} mA cm^{-2}) reduction in H_2 crossover with marginal decrease ~11% in areal proton conductance. Interestingly, when two layers of the slow growth graphene are stacked, H_2 crossover is reduced to record low values ~6.9×10^{-2} mA cm^{-2} (~83% reduction), while the proton transport only reduces by ~20%. Error bars represent one standard deviation. (G) Crossover current density for two N211||N211 membranes and stacked graphene membrane (N211|Graphene|Graphene|N211) with varying flow rates of N_2 ~ 16–40 sccm. A reduction in N_2 flow rate causes crossover in the control membranes to increase significantly but the effect is marginal for the N211|Graphene|Graphene|N211 membrane. (H) H_2 crossover current density (at 0.4 V) as a function of areal proton conductance for the centimeter-scale graphene membranes as well as other reports in literature (see Table S5). Open symbols represent as-measured values in this study (colored open symbols) as well as reports in literature (black open symbols). Filled colored symbols represent calculated areal proton conductance after subtraction of system resistance contribution, and filled stars represent the calculated areal proton conductance of graphene after subtraction of control membrane (N211||N211) resistance subtraction. The gray (stacked) and orange (N211||N211) horizontal dotted lines with arrow heads represent the range of crossover current densities measured using different flow rates of N_2 as shown in panel G (minimum crossover value ~2.5×10^{-2} m Acm^{-2} for stacked graphene). The graphene membranes exhibit significantly lower H_2 crossover while maintaining comparable proton transport to other materials such as Nafion,[2,3,6,38] SPEEK,[1−3] cellulose nanofibers[89] and SPEEK-$PtCs_{2.5}$[88] nanocomposites. Subtraction of the system and N211||N211resistance (see Experimental Methods and Table S4) indicates that the graphene is not the limiting resistance in our membranes, indicating kinetic control of angstrom scale defects and facile stacking approaches could enable practical advances toward the development of high flux proton exchange membranes with record low H_2 crossover.

https://doi.org/10.1021/acsnano.2c03730
ACS Nano 2022, 16, 16003−16018

provided the highest selectivity and so has the lowest value of $\bar{D}$. We allow the value of $\bar{D}$ to change with concentration because prior studies of ion transport through graphene have suggested that pH affects protonation of the graphene pores, thereby altering the pore size distribution.[86] The value of $\bar{D}$ decreases slightly as ion concentration increases.

Interestingly, two layers of graphene have an ion resistance of approximately twice that of one layer of graphene (Figure 4F). In contrast, gas transport resistances increase exponentially with the number of layers on PCTE supports, as each additional layer of graphene seals openings in the other layers.[78] This suggests that unlike gases, ions permeate the interlayer region between graphene sheets embedded in Nafion with low resistance (Figure 3L). However, the resistance increases with the distance traveled in the interlayer regions, as indicated by the higher H^+/K^+ selectivity when a second layer of graphene is added. We therefore propose that ions can permeate the stacked graphene membrane by passing through tears or defects in one layer of graphene, then moving laterally a short distance to pass through the nearby tears or defects in the second layer of graphene (Figure 4C, 3L). This gives four transport pathways contributing to the overall membrane resistance, as illustrated in Figure 4D (also see Figure 3L). The total resistance to passing through a membrane consisting of two layers of graphene between two Nafion layers is then

$$R_{2-\text{layer}} = 2R_{\text{nafion}} + \left(\frac{a^2}{2R_{\text{tears}}} + \frac{2a(1-a)}{R_{\text{tears}} + R_{\text{defects}}} + \frac{(1-a)^2}{2R_{\text{defects}}} \right)^{-1} \quad (6)$$

where a^2 gives the fraction of the area where two tears overlap, $(1-a)^2$ gives the fraction of the area where defective regions overlap (i.e., overlapping areas without tears), and $2a(1-a)$ gives the fraction of the area where tears and defects overlap.

This model captures the rise in resistance (Figure 4F) and selectivity (Figure 4G) when a second layer of graphene is added. This effectively reduces the fraction of the area with nonselective tears while increasing the area with selective defects. Several approximations have been made in the modeling. Using single fixed values for tear size, density, and area coverage neglects the distribution of tear size and variation between types of graphene. However, since these pores are not selective and the values chosen are in the physically expected range, the modeling confirms that the proposed mechanisms can explain the measurements. Pore conductance was approximated with a continuum expression while the smaller subnanometer defects are expected to deviate from these predictions.[84] The relation is still expected to provide the correct order of magnitude and it was decided that further refinement was not warranted since the pore size distribution used in the model was approximate and scaled to match measurements. Interlayer transport resistance is neglected over distances comparable to the tear diameter while transport over longer distances is neglected. More likely, the transport resistance increases continuously with distance traveled in the interlayer region and may be higher for K^+ than H^+, contributing to the higher selectivity of the stacked graphene. Nevertheless, the model is able to quantitatively explain the magnitude and trends in measured resistance and indicates conductance of ions between graphene layers as well as the significant contribution of defects to ion transport through large area graphene.

5. Proton Transport and H_2 Crossover through Centimeter-Scale Nafion|Graphene|Nafion PEM Membranes. Finally, we measure H^+ transport and H_2 crossover through the fabricated graphene-based PEMs to simulate the environment of a hydrogen fuel cell by using humidified H_2. Specifically, we aim to understand the implications of angstrom-scale defects introduced via facile kinetic control of graphene CVD on H^+ transport and H_2 crossover (Figure 5). Hence, the exact same membranes measured in the liquid phase are measured in the gas phase after adding Pt/C electrodes (see Experimental Methods), and we ensure the same membrane area probed in the liquid phase is loaded into the gas-phase system (Figure 5A), albeit the active area of the electrodes is smaller (~0.31 cm^2). The membrane resistance to H^+ transport is measured while humidified H_2 gas is supplied on both sides of the membrane (see Experimental Methods), and the current (I) is measured while sweeping the applied potential (V), resulting in $I-V$ curves (Figure 5B). The total membrane areal resistance upon adding a single layer of graphene increases by ~2.5×10^{-2} Ω cm^2, and when stacking an additional slow growth graphene layer, the total membrane areal resistance increases by ~4.8×10^{-2} Ω cm^2 as compared to the N211 sandwich control (Figure 5C and Table S4). Using the series resistance model to isolate the resistance contribution of graphene from that of the other components (Table S4), we calculate the areal proton conductance in the gas phase of ~39.9 S cm^{-2} (slow growth), ~57.7 S cm^{-2} (fast growth), and ~20.8 S cm^{-2} (stacked − 2 layers of slow growth graphene). Such high values of areal proton conductance for graphene after removing the contribution from Nafion and system resistance shows its adequacy for enabling practical applications in fuel cells, which typically require areal proton conductance values >1 S cm^{-2}.[40]

Additionally, we also measure crossover of H_2 gas (~2.9 Å), that is, leakage of H_2 gas through the membrane, which is a common problem affecting conventional PEM and results in reduced fuel cell efficiencies exacerbated over the application life-cycle as well as safety concerns in confined environments.[1,9,10] We use the same experimental setup (Figure 5A) but supply H_2 to one side of the membrane and N_2 gas to the other side.[9,10] At potential values below the open circuit potential, we observe the hydrogen evolution reaction (Figure S8) and at positive overpotentials above the open circuit potential, we measure current from dissociated H_2 which diffused through the membrane (Figure 5D). We note that these measurements of H_2 diffusion differ from our diffusion measurements of KCl and B12 in both support material (hydrated Nafion vs PCTE) and measurement method. There is a direct relationship between current density obtained in this limiting region and H_2 crossover which can be observed in the potential range from 0.1 to 0.5 V (Figure 5D). Here, we include a single layer of N211 to illustrate the relation between membrane thickness and crossover, i.e., higher crossover is seen for thinner Nafion membranes. For comparison between each of the synthesized CVD graphene types, we select the crossover current density at 0.4 V (Figure 5F) in accordance with the standard methods suggested by U.S. Department of Energy (U.S. DOE) as well as to ensure minimal influence from H^+ adsorption/desorption from the Pt catalyst.[9,10] The addition of graphene reduces the crossover current density from ~4.1×10^{-1} mA cm^{-2} (Nafion sandwich control) to ~1.7

https://doi.org/10.1021/acsnano.2c03730
ACS Nano 2022, 16, 16003−16018

$\times 10^{-1}$ mA cm^{-2} (slow growth), ~2.2 $\times 10^{-1}$ mA cm^{-2} (fast growth) and ~2.8 $\times 10^{-1}$ mA cm^{-2} (low T graphene). The crossover values obtained with graphene are lower than many literature values using other methods to reduce crossover e.g. using Pt-layered double hydroxide particles dispersed in Nafion (~7.5 $\times 10^{-1}$ mA cm^{-2}),[87] SPEEK-based nanocomposites (~7.7 $\times 10^{-1}$ mA cm^{-2}),[88] integrated cellulose fibers (~0.7 mA cm^{-2}), among others (Figure 5H, Table S5).[89]

Notably, we see substantial impact on H_2 crossover with the stacked slow growth graphene membrane, reduced to record low values of ~2.5 $\times 10^{-2}$ mA cm^{-2} which corresponds to ~90% reduction in H_2 crossover compared to the Nafion sandwich (Figure 5D−G). This large reduction in H_2 crossover comes at the expense of only ~20% reduction (Figure 5D−G) in proton transport compared to Nafion controls. Hydrogen crossover through the membrane is initially measured using similar flow rates of H_2 and N_2 on either side of the membrane, but we note that changing backpressure is a common strategy to mitigate H_2 crossover in an H_2 fuel cell.[9,10] Therefore, we explored the influence of different N_2 mass flow rates on the H_2 crossover and observed that lower amounts of N_2 led to an increase in H_2 crossover for the N211||N211 (presumably due to the lack of a sufficient back-pressure to mitigate H_2 diffusion[9]). Interestingly, H_2 crossover for the stacked graphene membrane remained very low (Figure 5G and Figure S9), i.e., the lowest value ~2.5 $\times 10^{-2}$ mA cm^{-2} for ~40 sccm of N_2 and ~40 sccm H_2 while the highest value was ~3.5 $\times 10^{-1}$ mA cm^{-2} for ~16 sccm N_2 and ~40 sccm H_2 (Table S6). These observations indicate the use of stacked slow growth graphene sandwich membranes could mitigate the need for applied backpressure when used in an H_2 fuel cell[9,10] as well as offer similar advantages for O_2 diffusion, thereby enhancing safety. Our observations indicate that the Angstrom-scale defects in the graphene layers allow for selective H^+ transport while still blocking molecular H_2 (~2.9 Å) and still exhibit adequate H^+ conductance ~20.8 S cm^{-2}, i.e. the defect density of the stacked slow graphene is adequate to prevent diffusion of H_2 while electrically driven protons can continue to move at a rapid rate. Hence, we emphasize the application potential of our facile method of stacking graphene layers, which can be readily integrated into PEMs for enabling higher efficiency in fuel cell applications.

CONCLUSIONS

In conclusion, we demonstrated that facile kinetic control of the scalable graphene CVD processes can be leveraged to introduce angstrom-scale pores that allow for enhanced proton transport while simultaneously presenting significant hindrance to even small, hydrated ions (K^+ ~6.6 Å) as well as gas molecules (H_2 ~2.9 Å). We experimentally probe the influence of the introduced angstrom-scale defects and demonstrate centimeter-scale Nafion|Graphene|Nafion membranes with proton conductance ~3.3−3.8 S cm^{-2} (graphene only ~12.7−24.6 S cm^{-2}), H^+/K^+ selectivity ~6.2−44.2 in liquid electrolytes, and the same membranes show proton conductance ~4.6−4.8 S cm^{-2} (graphene only ~39.9−57.5 S cm^{-2}) with H_2 crossover ~0.17−0.22 mA cm^{-2} (~0.4 V, ~25 °C) while using H_2 gas as the proton source. We develop a resistance-based transport model to explain the observed transport and introduce a graphene stacking approach for facile and scalable membrane fabrication. Our stacking approach exploits the combinatorial effects of inter-defect distance and inter-layer transport to allow for Nafion|Graphene|Graphene| Nafion membranes with record low H_2 crossover current density (~2.5 $\times 10^{-2}$ mA cm^{-2} and H^+/K^+ selectivity ~86.1 at 1 M), ~90% lower than state-of-the-art ionomer Nafion membranes (~2.7 $\times 10^{-1}$ mA cm^{-2}) under identical conditions, while still maintaining proton conductance (~4.2 S cm^{-2}, graphene stack only ~20.8 S cm^{-2}) comparable to Nafion (~5.2 S cm^{-2}). We expect our insights on facile kinetic control of scalable CVD processes for direct formation of angstrom-scale proton-selective pores and facile stacking approaches for scalable membrane fabrication to enable functional atomically thin high flux proton exchange membranes with transformative advances for PEMs in energy conversion, energy storage, challenging separations among others to advance clean/green/decarbonized transportation, grid storage and other climate change mitigation efforts.

EXPERIMENTAL METHODS

Graphene Growth. Graphene was synthesized using a custom-built hot-wall reactor with 1 in. quartz tube and furnace using procedures described elsewhere.[28,30−34,49] Details of temperature, H_2 mass flow rate, and CH_4 mass flow rate for each graphene type are shown in Figure S1. Briefly, ~2 × 7 cm^2 polycrystalline Cu foil (HA, 18 μm thickness, JX Holdings) was cleaned via sonication in 20 v/v% Nitric Acid for 4 min followed by thorough DI water rinse and air-dried before loading into the reactor and pumping down to base pressure (~14 mTorr). H_2 (99.999%, AL Gas) and CH_4 (99.9%, AL Gas) gas mass flow rates are controlled with mass flow controllers. The growth process consists of heating (~35 °C/min) to 1060 °C in ~100 sccm H_2 (system pressure ~4 Torr) followed by annealing (1060 °C; 100 sccm H_2, 60 min) to reduce surface oxide and enlarge the Cu grain size. After annealing for 60 min with 100 sccm H_2 and before the introduction of methane, the temperature is reduced to 900 °C under 60 sccm H_2 and maintained for 30 min for the low T growth and for the slow growth the H_2 flow rate is increased to 300 sccm H_2 for 15 min. Methane is introduced in 2 steps: (i) slow growth graphene: 1060 °C, 300 sccm H_2 (~14 Torr), growth step #1 with 0.5 sccm CH_4 for 60 min (~12 Torr), growth step #2 with 1 sccm CH_4 for 30 min (~12 Torr); (ii) fast growth graphene: 1060 °C, 100 sccm H_2 (~4 Torr), growth step #1 with 2 sccm CH_4 for 30 min (~2 Torr), growth step #2 with 4 sccm CH_4 for 30 min (~2 Torr); (iii) Low T graphene: 900 °C, 60 sccm H_2 (~1 Torr), growth step #1 with 3.5 sccm for 30 min CH_4 (~900 mTorr), growth step #2 with 7 sccm CH_4 for 30 min (~850 mTorr)[31,32,34] and then quench cooled to room temperature in the final growth atmosphere.

Graphene Coverage and Nucleation Density from Scanning Electron Microscopy Images. Using the step #1 flow rates, slow, fast, and low T graphene growth times were varied between 30 s to 60 min to stop the growth at various stages of domain convergence (Figure 1). Graphene coverage and nucleation density were estimated from SEM images (Zeiss Merlin, 2 kV) of graphene on Cu using ImageJ software to threshold the images by color or contrast, then "particle analysis" to count the graphene domains and calculate the total area covered (Figure S2). Nucleation density (Figure 1C) was calculated from SEM images of 30 s fast graphene, 30 s low T graphene, and 5 min slow graphene as the domains had not yet converged and could be counted.

Optical Images of Graphene on Cu Foil after Thermal Oxidation. Optical images of graphene domains were acquired at 10× and 50× magnification after thermal oxidation of graphene on Cu foil. Samples were heated for 15 min on a hot plate at 220 °C to oxidize exposed Cu, i.e., region between unmerged graphene domains and at graphene defects.[25]

Electrochemical and Acid Etch Tests. Electrochemical etch and acid etch tests were used to estimate the defect density of slow, fast, and low T graphene as described in detail elsewhere.[30] Briefly, the electrochemical etch test (Figure 1D) was performed using a two-electrode geometry, with the working electrode connected to slow, fast, and low T graphene on Cu foil (~0.5 × 1 cm^2) and the

https://doi.org/10.1021/acsnano.2c03730
ACS Nano 2022, 16, 16003−16018

reference/counter electrode connected to bare Cu foil (~1 × 5 cm^2). Both Cu foils with (smaller) and without graphene (larger) electrodes were submerged in 0.5 M $CuSO_4$, while 1 V was applied between the electrodes for 1 s.[30] The graphene on Cu foil was then rinsed thoroughly in DI water, dried and imaged with SEM.[30] For the acid etch tests, a droplet ~5 μL of 0.1 M Iron Chloride ($FeCl_3$) solution was placed on the surface of slow, fast, and low T graphene on Cu foil for 2 s (Figure S3) then rinsed thoroughly with DI water to stop the etching, dried, and images with SEM.[30] Etched regions appear as bright, white spots in SEM images and ImageJ software was used to calculate the total area etched and defect density (Figure 1D) by thresholding and using particle analysis.

Raman Spectroscopy. Graphene was transferred to SiO_2/Si wafer (300 nm SiO_2) using a poly methyl methacrylate (PMMA) assisted method.[33,34,49] PMMA solution (MW 35000, 2 wt % in anisole) was drop cast on top of slow, fast, and low T graphene on Cu and dried at ambient conditions. The graphene is first pre-etched in ammonium persulfate solution (APS, 0.2 M) for 15 min and rinsed with DI water to remove the bottom layer of graphene before fully etching the Cu in APS solution (0.2 M). The graphene/PMMA stack is then rinsed in DI water and scooped onto the SiO_2/Si wafer. After baking at 60 °C for 10 min, the PMMA layer is removed by rinsing in acetone and IPA. Raman spectra (ThermoFisher DXR Confocal Raman Microscope, 532 nm laser) were then recorded for slow, fast, and low T graphene (Figure B) using 1 mW laser power.

Scanning Tunnelling Microscopy (STM). An Omicron LT-Nanoprobe scanning tunneling microscope at the Center for Nanophase Materials Sciences at Oak Ridge National Laboratory was used to acquire STM images at 4.6 K. *In situ* SEM that is attached to the STM chamber was utilized to position the STM tip over the graphene nuclei. The as-synthesized graphene on Cu was annealed under ultrahigh vacuum (<3 × 10^{-10} mbar) at 420 °C for 3 h before imaging.

Graphene Transfer onto PCTE. Graphene was transferred to polycarbonate track-etched (PCTE, Sterlitech) supports with ~200 nm pores and ~10% porosity via isopropanol assisted hot lamination.[34] As with the PMMA assisted transfer, the bottom layer of graphene was first removed by pre-etching in ammonium persulfate (APS, 0.2 M) solution for 15 min, followed by DI water rinse and dried in air.[28,30−32,34] Next, the PCTE support was placed against the graphene+Cu foil with the graphene side facing up. Subsequently, a small volume (~50 μL) of isopropanol was added to the PCTE +graphene interface. The PCTE+graphene+Cu stack was then sandwiched between two pieces of weighing paper and laminated with Teflon protective layers at 135 °C with an office laminator (TruLam TL-320E). After lamination, the Cu foil was completely etched by floating the PCTE+graphene+Cu stack on APS (0.2 M) solution. Finally, the PCTE+graphene stack was rinsed with DI water and ethanol, followed by drying in air.

Pressure- and Diffusion-Driven Solute Transport Measurements. Pressure-driven ethanol and diffusion-driven solute transport measurements across the fabricated PCTE+graphene membranes were performed as reported previously.[28,30−34,42,85] A custom-made side-by-side glass diffusion cell (7 mL, 5 mm orifice, PermeGear, Inc.) with a gastight syringe (250 μL, Hamilton 1725 Luer Tip) installed onto the open port of the left cell (feed side, sealed with epoxy for leak-free connection) as shown in Figure S4A was used for both pressure-driven and diffusion-driven transport measurements. The PCTE+graphene membrane was installed between two diffusion cells with the graphene side facing left. To minimize the concentration polarization, two Teflon coated stir bars stirred vigorously in both cells.

For pressure-driven ethanol transport measurement (Figure S4B),[30,31,33,34] pure ethanol was used to wash the system three times before filling both cells with pure ethanol. The left cell (feed side) was sealed by a rubber plug to raise the ethanol level in the syringe, thereby creating a hydrostatic pressure difference across the membrane. A digital camera was used to record the ethanol meniscus level change along the syringe every 1 min. The ethanol permeance was calculated by permeance = $(\Delta V/\Delta P)/(\Delta t \times A_{effective})$, where ΔV is the ethanol volume change, ΔP is the hydrostatic pressure difference across the membrane, Δt is the time interval (1 min), and $A_{effective}$ is the effective membrane area (~0.196 cm^2). The ethanol coverage was computed by coverage = [1 − (PCTE) + graphene ethanol permeance)/(PCTE ethanol permeance)] × 100.[30,33,34,85]

After pressure-driven ethanol transport measurement, the system was washed with DI water five times to completely replace ethanol. KCl (Fisher Chemical, 7447-40-7, salt, hydrated diameter of K^+ ~0.66 nm and Cl^- ~0.66 nm),[25] and Vitamin B12 (B12, Sigma-Aldrich, 68-19-9, vitamin, ~1−1.5 nm)[30] were used for measuring diffusion-driven transport. For KCl transport measurements,[28,30−34,42,85] 7 mL of KCl solution (0.5 M in DI water) was filled into the feed side and 7 mL of DI water was filled into the permeate side. A conductivity probe (Mettler Toledo SevenCompact S230 conductivity meter) was immersed in the permeate side to collect the conductivity every 15 s for 15 min. For B12 transport measurement,[28,30−34,42,85] 7 mL of B12 solution (1 mM in 0.5 M KCl) was filled into the feed side and 7 mL of KCl solution (0.5 M) was filled into the permeate side. A fiber optic dip probe attached to an Agilent Cary 60 UV−vis Spectrophotometer was immersed in the permeate side to record the absorbance spectra in the range of 190 to 1100 nm every 15 s for 40 min. Different UV−vis peak positions were used for measuring the intensity differences of corresponding species: 710 nm for DI water (reference wavelength),[28,30−34,42,85] and 360 nm for B12.[28,30−34,42,85] The flow rate of each solute was computed via the slope of concentration change in the permeate side (right cell), while the normalized flux was computed by dividing the slope of the PCTE +graphene membrane by that of the PCTE support.[28,30−34,42,85] All the measurements were replicated three times to obtain average values and standard deviations.[28,30−34,42,85]

Nafion|Graphene|Nafion Membrane Fabrication. Graphene is transferred to Nafion using similar methods to others developed previously.[37−40] Nafion 211 (N211, ~25 μm thickness, Fuel Cell Store) is first converted from the acid form (as received) to salt form (K^+) by soaking in KCl (0.1M) solution at room temperature. After 1 h the pH of the KCl solution is checked and solution exchanged with fresh KCl (0.1M) until the pH is no longer acidic. After ~3 exchanges, the N211 is heated to 80 °C for 1 h in KCl solution (0.1M) then kept in KCl solution for 48 h to ensure complete exchange of the N211 membranes to salt form (N211-K^+). Finally, the N211 is rinsed with DI water and dried.

Graphene on Cu is cut to ~2.25 cm^2 pieces and N211-K^+ is placed on top. A thin layer of Nafion solution (1100 MW, 1 wt %) is applied to a PTFE-coated fiberglass mat (15 mil thickness) and placed on the N211-K^+.[90] An additional fiberglass mat is placed on the bottom, below the graphene on Cu and the whole stack is hot pressed at 145 °C for 3 min at ~1000 psi. The bottom fiberglass mat is removed and the remaining Cu|Graphene|N211-K^+|fiberglass stack is pre-etched in APS solution (0.2 M) for 15 min and rinsed in DI water to remove the bottom layer of graphene from the Cu. The stack is returned to APS (0.2 M) solution to fully etch away the Cu then rinsed with DI water for 10 min, dried in air at ambient conditions, then dried at 60 °C for 12 h. Finally, a second N211-K^+ layer is hot-pressed on top of the graphene (145 °C, 3 min, ~1000 psi) to form a Nafion|Graphene|Nafion sandwich membrane.

The stacked graphene membrane is prepared using a similar procedure. Here, a thin layer of Nafion is spin coted on the graphene on Cu foil. The thin Nafion film is formed by spin coating three layers of Nafion solution (1× 5 wt %, 2× 1 wt %, 1000 rpm, 60 s) then drying at 60 °C for 10 min between layers and 30 min after the third layer. The bottom layer of graphene on Cu is removed using the same pre-etching conditions and the Cu fully etched in APS (0.2 M) solution. Once etched, the Graphene|Nafion stack is transferred to a DI water bath for 10 min, then to a fresh DI water bath before scooping it onto another piece of graphene on Cu foil, making a Cu|Graphene|Graphene|Nafion stack. The stack is dried at 60 °C for 12 h before pre-etching and fully etching the Cu as previously described. Finally, the Graphene|Graphene|Nafion stack is rinsed in DI water before scooping onto N211-K^+. After drying at 80 °C for 12 h, an

https://doi.org/10.1021/acsnano.2c03730
ACS Nano 2022, 16, 16003−16018

additional N211 layer is added to the stack and hot pressed to form a Nafion|Graphene|Graphene|Nafion (stacked) sandwich membrane.

Electrically Driven Ion Transport Measurements with Liquid Electrolytes in H-Cell. Electrically driven ion transport in the liquid phase is measured using a custom-built H-Cell (Figure S6A) with the membrane placed between two electrolyte reservoirs. Luggin capillaries are positioned ∼0.6 mm from the membrane on either side. Ag/AgCl pellet electrodes (A-M systems) at the far end of the Luggin capillaries are used to measure potential while current is driven by Pt wire (Alfa Aesar, 0.23 in. D) coiled around the capillaries. The open orifice area (membrane area probed) is ∼0.68 cm^2. Approximately, 6 mL of solution (KCl or HCl) is added to either reservoir for measurements.

Current/Voltage (*IV*) curves are obtained using a potentiostat (Gamry, Interface 1010B) in a four-probe geometry (working and counter electrodes on Pt wires, working sense and reference electrodes on the Ag/AgCl pellets). Multiple-step chronoamperometry is used to set and hold the cell potential (from ±60 mV, step size 10 mV) for 30 s to allow for steady-state measurements of current at the applied potential (Figure S6B). The measured current (taken as the last measurement at each potential step) is plotted versus voltage to obtain a linear *IV* curve. We estimate the conductance of the membrane from the slope of the *IV* curve. The conductance is related to membrane resistance by $\sigma = 1/R$.

K^+ transport using KCl (0.1M, 0.5M, and 1 M) is measured first before exchanging the membrane to acid form by soaking in HCl (0.1 M) for 1 h, exchanging with fresh HCl (0.1 M) for another hour, then exchanging with fresh HCl (0.1 M) again and leaving for 48 h (Figure S7). The same multistep-chronoamperometry method is used to obtain *IV* curves with HCl (0.1, 0.5, and 1 M) for H^+ transport. Areal conductance is obtained by dividing the conductance by the open membrane area. Normalized K^+ flux is calculated as normalized K^+ flux = (average Nafion|Graphene|Nafion K^+ conductance)/(average Nafion||Nafion K^+ conductance). Membrane H^+/K^+ selectivity is calculated as the ratio of average areal H^+ conductance through the membrane divided by the average areal K^+ conductance through the membrane. Error bars represent one standard deviation and account for error propagation.

Gas-Phase Proton Transport Measurements. After measuring K^+ and H^+ transport in the liquid phase in the H-cell, areal proton conductance through the membrane is measured using H_2 gas as the proton source. The membranes are rinsed in deionized water and dried for 24 h in ambient conditions before adding platinum carbon electrodes (Pt/C, 1/4 in. diameter, ∼0.38 cm^2, 0.2 mg Pt cm^{-2} loading). Pt/C electrodes are positioned in the center of the region which was tested in the liquid phase and hot-pressed on either side of the membrane, so the same region is probed in the gas phase as the liquid phase measurements. The membrane is loaded into a custom-built gas cell similar in design to previous reports.[36−38] The gas cell comprises of a PTFE compression fitting, graphite rod current collectors with channels for gas inlet and outlet, rubber gaskets to seal the membranes and porous Ni foam electrical contacts (Figure 5A).

For measuring H^+ transport, humidified H_2 gas (99.999%, ∼40 sccm bubbling through DI water before entering the cell) is supplied to either side of the membrane. We refer to this configuration as symmetric mode. The potentiostat leads are connected to the graphite rod current collectors in a two-probe geometry (working and working sense electrodes on one side, while the counter and reference electrodes are on the other side). Linear sweep voltammetry (LSV) is used, sweeping the applied potential from ±60 mV at a scan rate of 2 mV/s. The membrane areal H^+ conductance and areal resistance are calculated from the resulting linear *IV* curve. The percent H^+ transport reduction is calculated as percent reduction = {(Nafion|| Nafion conductance − Nafion|Graphene|Nafion conductance)/(Nafion||Nafion conductance)] × 100. Error bars represent one standard deviation and account for error propagation.

H_2 Crossover Current Density Measurements. H_2 crossover is also measured in the gas phase cell at room temperature with 40 sccm humidified H_2 gas supplied to one side of the membrane and varying flow rates ∼16−40 sccm of humidified N_2 gas (99.9%) supplied to the other. We refer to this configuration as asymmetric mode. Initially all membranes, that is, N211, N211||N211, fast, slow, low T, and stacked were measured under identical flow conditions ∼40 sccm H_2 and ∼32 sccm N_2. To test the H_2 crossover of the N211||N211 and stack membrane, the H_2 flow rate was kept at ∼40 sccm while the N_2 flow rate was systematically varied between ∼16−40 sccm. LSV is measured from 0.5−0 V with a two-probe geometry (working and working sense electrodes on the N_2 side; the counter and reference electrodes on the H_2 side). In this configuration, H_2 which diffused through the membrane (crossover) is oxidized at the anode (N_2 side) into protons and driven back through the membrane via the applied potential. The recombination of these H^+ on the H_2 side (cathode) is measured as current, generally referred to as the limiting current (I_{lim}) and used as a measure of H_2 crossover.[9,10] The limiting current for each membrane is taken at 0.4 V (DOE standard method)[9,10] as this region is free from influence of H^+ adsorption/desorption to the Pt. Crossover current density is obtained by dividing the limiting current at 0.4 V by the active area (∼0.318 cm^2). The percent H_2 crossover reduction for each graphene membrane is calculated as percent reduction = {[I_{lim}(Nafion||Nafion) − I_{lim}(Nafion|Graphene|Nafion)]/I_{lim}(Nafion||Nafion)} × 100. Error bars represent one standard deviation and account for error propagation.

ASSOCIATED CONTENT

Supporting Information

The Supporting Information is available free of charge at https://pubs.acs.org/doi/10.1021/acsnano.2c03730.

Graphene synthesis conditions, acid etch test, calculations of graphene nucleation density and coverage, pressure-driven characterization of graphene transfer to PCTE, SEM of graphene on Nafion, electrochemical methods for measuring transport in liquid electrolytes, confirmation of Nafion pretreatment method, extended I−V curve for H_2 crossover, effect of variable N_2 flow on crossover, calculations of resistance and conductance for membranes and graphene only with 0.1, 0.5, and 1 M KCl and HCl, selectivity calculations at 0.1, 0.5 and 1 M, calculations of resistance and conductance for membranes and graphene only in gas phase, comparison of crossover and membrane areal conductance, and table of crossover values obtained with variable N_2 flow rates (PDF)

AUTHOR INFORMATION

Corresponding Author

Piran R. Kidambi − *Department of Chemical and Biomolecular Engineering and Department of Mechanical Engineering, Vanderbilt University, Nashville, Tennessee 37212, United States; Vanderbilt Institute of Nanoscale Science and Engineering, Nashville, Tennessee 37212, United States;* orcid.org/0000-0003-1546-5014; Email: piran.kidambi@vanderbilt.edu

Authors

Nicole K. Moehring − *Interdisciplinary Graduate Program in Materials Science, Vanderbilt University, Nashville, Tennessee 37235, United States; Department of Chemical and Biomolecular Engineering, Vanderbilt University, Nashville, Tennessee 37212, United States; Vanderbilt Institute of Nanoscale Science and Engineering, Nashville, Tennessee 37212, United States*

Pavan Chaturvedi − *Department of Chemical and Biomolecular Engineering, Vanderbilt University, Nashville, Tennessee 37212, United States; Vanderbilt Institute of*

https://doi.org/10.1021/acsnano.2c03730
ACS Nano 2022, 16, 16003−16018

Nanoscale Science and Engineering, Nashville, Tennessee 37212, United States

Peifu Cheng − *Department of Chemical and Biomolecular Engineering, Vanderbilt University, Nashville, Tennessee 37212, United States; Vanderbilt Institute of Nanoscale Science and Engineering, Nashville, Tennessee 37212, United States*

Wonhee Ko − *Center for Nanophase Materials Sciences, Oak Ridge National Laboratory, Oak Ridge, Tennessee 37831, United States*

An-Ping Li − *Center for Nanophase Materials Sciences, Oak Ridge National Laboratory, Oak Ridge, Tennessee 37831, United States;* orcid.org/0000-0003-4400-7493

Michael S. H. Boutilier − *Department of Chemical and Biochemical Engineering, Western University, London, Ontario N6A 3K7, Canada;* orcid.org/0000-0001-6309-2318

Complete contact information is available at: https://pubs.acs.org/10.1021/acsnano.2c03730

Author Contributions

P.R.K. designed and supervised the project. N.K.M. performed the experiments and analyzed the results. Peifu Cheng [P.C.#1] performed diffusion and pressure-driven transport measurements. N.K.M, P.R.K., P.C.#1 and Pavan Chaturvedi [P.C.#2] interpreted the results. M.S.H.B. developed the mathematical transport model and wrote the corresponding parts of the manuscript. W.K. and A.P.L. performed STM measurements. N.K.M. and P.R.K. wrote the manuscript with input and revisions from all authors.

Notes

The authors declare the following competing financial interest(s): P.R.K. declares stake in a company aimed at commercializing 2D materials.

ACKNOWLEDGMENTS

This research was supported in part by the U.S. Department of Energy Isotope Program, managed by the Office of Science for Isotope R&D and Production under award number DE-SC0022237, in part by faculty start-up funds from Vanderbilt University to P.R.K, and in part by NSF CAREER award #1944134. P.R.K. acknowledges the ECS Toyota Young Investigator Fellowship. The STM imaging was performed at the Center for Nanophase Materials Sciences at Oak Ridge National Laboratory, a U.S. Department of Energy Office of Science User Facility. The use of Vanderbilt Institute of Nanoscale Science and Engineering CORE facilities are acknowledged. N.K.M and P.R.K. would like to thank and acknowledge helpful scientific discussions and insights from Prof. Peter Pintauro and Dr. Krysta Waldrop.

REFERENCES

(1) Kidambi, P. R.; Chaturvedi, P.; Moehring, N. K. Subatomic Species Transport through Atomically Thin Membranes: Present and Future Applications. *Science* **2021**, *374* (6568), eabd7687.

(2) Wang, Y.; Ruiz Diaz, D. F.; Chen, K. S.; Wang, Z.; Adroher, X. C. Materials, Technological Status, and Fundamentals of PEM Fuel Cells − A Review. *Mater. Today* **2020**, *32*, 178−203.

(3) Junoh, H.; Jaafar, J.; Nik Abdul, N. A. H.; Ismail, A. F.; Othman, M. H. D.; Rahman, M. A.; Aziz, F.; Yusof, N. Performance of Polymer Electrolyte Membrane for Direct Methanol Fuel Cell Application: Perspective on Morphological Structure. *Membranes (Basel)* **2020**, *10* (3), 34.

(4) Tempelman, C. H. L.; Jacobs, J. F.; Balzer, R. M.; Degirmenci, V. Membranes for All Vanadium Redox Flow Batteries. *J. Energy Storage* **2020**, *32*, 101754.

(5) Satyapal, S.*DOE Hydrogen and Fuel Cell Perspectives and Overview of the International Partnership for Hydrogen and Fuel Cells in the Economy (IPHE)*; Presented at Global America Business Institute (GABI) Virtual Workshop, July 1, 2020U.S. Department of Energy Hydrogen and Fuel Cells Program, 2020.

(6) Slade, S.; Campbell, S. A.; Ralph, T. R.; Walsh, F. C. Ionic Conductivity of an Extruded Nafion 1100 EW Series of Membranes. *J. Electrochem. Soc.* **2002**, *149* (12), A1556.

(7) Klose, C.; Saatkamp, T.; Münchinger, A.; Bohn, L.; Titvinidze, G.; Breitwieser, M.; Kreuer, K.; Vierrath, S. All-Hydrocarbon MEA for PEM Water Electrolysis Combining Low Hydrogen Crossover and High Efficiency. *Adv. Energy Mater.* **2020**, *10* (14), 1903995.

(8) Jiang, R.; Kunz, H. R.; Fenton, J. M. Investigation of Membrane Property and Fuel Cell Behavior with Sulfonated Poly(Ether Ether Ketone) Electrolyte: Temperature and Relative Humidity Effects. *J. Power Sources* **2005**, *150* (1−2), 120−128.

(9) Inaba, M.; Kinumoto, T.; Kiriake, M.; Umebayashi, R.; Tasaka, A.; Ogumi, Z. Gas Crossover and Membrane Degradation in Polymer Electrolyte Fuel Cells. *Electrochim. Acta* **2006**, *51* (26), 5746−5753.

(10) Schoemaker, M.; Misz, U.; Beckhaus, P.; Heinzel, A. Evaluation of Hydrogen Crossover through Fuel Cell Membranes. *Fuel Cells* **2014**, *14* (3), 412−415.

(11) Hu, S.; Lozada-Hidalgo, M.; Wang, F. C.; Mishchenko, A.; Schedin, F.; Nair, R. R.; Hill, E. W.; Boukhvalov, D. W.; Katsnelson, M. I.; Dryfe, R. A. W.; Grigorieva, I. v.; Wu, H. A.; Geim, A. K. Proton Transport through One-Atom-Thick Crystals. *Nature* **2014**, *516* (7530), 227−230.

(12) Bunch, J. S.; Verbridge, S. S.; Alden, J. S.; van der Zande, A. M.; Parpia, J. M.; Craighead, H. G.; Mceuen, P. L. Impermeable Atomic Membranes from Graphene Sheets. *Nano Lett.* **2008**, *8* (8), 2458−2462.

(13) Sun, P. Z.; Yang, Q.; Kuang, W. J.; Stebunov, Y. v.; Xiong, W. Q.; Yu, J.; Nair, R. R.; Katsnelson, M. I.; Yuan, S. J.; Grigorieva, I. v.; Lozada-Hidalgo, M.; Wang, F. C.; Geim, A. K. Limits on Gas Impermeability of Graphene. *Nature* **2020**, *579* (7798), 229−232.

(14) Yan, X. H.; Wu, R.; Xu, J. B.; Luo, Z.; Zhao, T. S. A Monolayer Graphene − Nafion Sandwich Membrane for Direct Methanol Fuel Cells. *J. Power Sources* **2016**, *311*, 188−194.

(15) Bukola, S.; Creager, S. E. Graphene-Based Proton Transmission and Hydrogen Crossover Mitigation in Electrochemical Hydrogen Pump Cells. *ECS Trans.* **2019**, *92* (8), 439−444.

(16) Bukola, S.; Li, Z.; Zack, J.; Antunes, C.; Korzeniewski, C.; Teeter, G.; Blackburn, J.; Pivovar, B. Single-Layer Graphene as a Highly Selective Barrier for Vanadium Crossover with High Proton Selectivity. *J. Energy Chem.* **2021**, *59*, 419−430.

(17) Yoon, S. I.; Seo, D.-J.; Kim, G.; Kim, M.; Jung, C.-Y.; Yoon, Y.-G.; Joo, S. H.; Kim, T.-Y.; Shin, H. S. AA′-Stacked Trilayer Hexagonal Boron Nitride Membrane for Proton Exchange Membrane Fuel Cells. *ACS Nano* **2018**, *12* (11), 10764−10771.

(18) Holmes, S. M.; Balakrishnan, P.; Kalangi, V. S.; Zhang, X.; Lozada-Hidalgo, M.; Ajayan, P. M.; Nair, R. R. 2D Crystals Significantly Enhance the Performance of a Working Fuel Cell. *Adv. Energy Mater.* **2017**, *7* (5), 1601216.

(19) Lozada-Hidalgo, M.; Zhang, S.; Hu, S.; Kravets, V. G.; Rodriguez, F. J.; Berdyugin, A.; Grigorenko, A.; Geim, A. K. Giant Photoeffect in Proton Transport through Graphene Membranes. *Nat. Nanotechnol.* **2018**, *13* (4), 300−303.

(20) Lozada-Hidalgo, M.; Hu, S.; Marshall, O.; Mishchenko, A.; Grigorenko, A. N.; Dryfe, R. A. W.; Radha, B.; Grigorieva, I. v.; Geim, A. K. Sieving Hydrogen Isotopes through Two-Dimensional Crystals. *Science* **2016**, *351* (6268), 68−70.

(21) Mogg, L.; Zhang, S.; Hao, G. P.; Gopinadhan, K.; Barry, D.; Liu, B. L.; Cheng, H. M.; Geim, A. K.; Lozada-Hidalgo, M. Perfect Proton Selectivity in Ion Transport through Two-Dimensional Crystals. *Nat. Commun.* **2019**, *10* (1), 4243.

(22) Griffin, E.; Mogg, L.; Hao, G.-P.; Kalon, G.; Bacaksiz, C.; Lopez-Polin, G.; Zhou, T. Y.; Guarochico, V.; Cai, J.; Neumann, C.; Winter, A.; Mohn, M.; Lee, J. H.; Lin, J.; Kaiser, U.; Grigorieva, I. v.; Suenaga, K.; Özyilmaz, B.; Cheng, H.-M.; Ren, W.; Turchanin, A.; Peeters, F. M.; Geim, A. K.; Lozada-Hidalgo, M. Proton and Li-Ion Permeation through Graphene with Eight-Atom-Ring Defects. *ACS Nano* **2020**, *14* (6), 7280−7286.
(23) Koenig, S. P.; Boddeti, N. G.; Dunn, M. L.; Bunch, J. S. Ultrastrong Adhesion of Graphene Membranes. *Nat. Nanotechnol.* **2011**, *6* (9), 543−546.
(24) Wang, L.; Williams, C. M.; Boutilier, M. S. H.; Kidambi, P. R.; Karnik, R. Single-Layer Graphene Membranes Withstand Ultrahigh Applied Pressure. *Nano Lett.* **2017**, *17* (5), 3081−3088.
(25) Wang, L.; Boutilier, M. S. H.; Kidambi, P. R.; Jang, D.; Hadjiconstantinou, N. G.; Karnik, R. Fundamental Transport Mechanisms, Fabrication and Potential Applications of Nanoporous Atomically Thin Membranes. *Nat. Nanotechnol.* **2017**, *12* (6), 509−522.
(26) Prozorovska, L.; Kidambi, P. R. State-of-the-Art and Future Prospects for Atomically Thin Membranes from 2D Materials. *Adv. Mater.* **2018**, *30* (52), 1801179.
(27) Chaturvedi, P.; Vlassiouk, I. v.; Cullen, D. A.; Rondinone, A. J.; Lavrik, N. v.; Smirnov, S. N. Ionic Conductance through Graphene: Assessing Its Applicability as a Proton Selective Membrane. *ACS Nano* **2019**, *13* (10), 12109−12119.
(28) Kidambi, P. R.; Mariappan, D. D.; Dee, N. T.; Vyatskikh, A.; Zhang, S.; Karnik, R.; Hart, A. J. A Scalable Route to Nanoporous Large-Area Atomically Thin Graphene Membranes by Roll-to-Roll Chemical Vapor Deposition and Polymer Support Casting. *ACS Appl. Mater. Interfaces* **2018**, *10* (12), 10369−10378.
(29) Kobayashi, T.; Bando, M.; Kimura, N.; Shimizu, K.; Kadono, K.; Umezu, N.; Miyahara, K.; Hayazaki, S.; Nagai, S.; Mizuguchi, Y.; Murakami, Y.; Hobara, D. Production of a 100-m-Long High-Quality Graphene Transparent Conductive Film by Roll-to-Roll Chemical Vapor Deposition and Transfer Process. *Appl. Phys. Lett.* **2013**, *102* (2), 023112.
(30) Kidambi, P. R.; Terry, R. A.; Wang, L.; Boutilier, M. S. H.; Jang, D.; Kong, J.; Karnik, R. Assessment and Control of the Impermeability of Graphene for Atomically Thin Membranes and Barriers. *Nanoscale* **2017**, *9* (24), 8496−8507.
(31) Cheng, P.; Kelly, M. M.; Moehring, N. K.; Ko, W.; Li, A.-P.; Idrobo, J. C.; Boutilier, M. S. H.; Kidambi, P. R. Facile Size-Selective Defect Sealing in Large-Area Atomically Thin Graphene Membranes for Sub-Nanometer Scale Separations. *Nano Lett.* **2020**, *20* (8), 5951−5959.
(32) Kidambi, P. R.; Nguyen, G. D.; Zhang, S.; Chen, Q.; Kong, J.; Warner, J.; Li, A.-P. P.; Karnik, R. Facile Fabrication of Large-Area Atomically Thin Membranes by Direct Synthesis of Graphene with Nanoscale Porosity. *Adv. Mater.* **2018**, *30* (49), 1804977.
(33) Kidambi, P. R.; Boutilier, M. S. H.; Wang, L.; Jang, D.; Kim, J.; Karnik, R. Selective Nanoscale Mass Transport across Atomically Thin Single Crystalline Graphene Membranes. *Adv. Mater.* **2017**, *29* (19), 1605896.
(34) Cheng, P.; Moehring, N. K.; Idrobo, J. C.; Ivanov, I. N.; Kidambi, P. R. Scalable Synthesis of Nanoporous Atomically Thin Graphene Membranes for Dialysis and Molecular Separations via Facile Isopropanol-Assisted Hot Lamination. *Nanoscale* **2021**, *13* (5), 2825−2837.
(35) Ullah, S.; Yang, X.; Ta, H. Q.; Hasan, M.; Bachmatiuk, A.; Tokarska, K.; Trzebicka, B.; Fu, L.; Rummeli, M. H. Graphene Transfer Methods: A Review. *Nano Research* **2021**, *14* (11), 3756−3772.
(36) Bukola, S.; Creager, S. E. A Charge-Transfer Resistance Model and Arrhenius Activation Analysis for Hydrogen Ion Transmission across Single-Layer Graphene. *Electrochim. Acta* **2019**, *296*, 1−7.
(37) Bukola, S.; Cao, D.; Martinson, A. B. F.; Creager, S. Effects of Atomic-Layer-Deposition Alumina on Proton Transmission through Single-Layer Graphene in Electrochemical Hydrogen Pump Cells. *ACS Appl. Energy Mater.* **2020**, *3* (2), 1364−1372.
(38) Bukola, S.; Liang, Y.; Korzeniewski, C.; Harris, J.; Creager, S. Selective Proton/Deuteron Transport through Nafion|Graphene|Nafion Sandwich Structures at High Current Density. *J. Am. Chem. Soc.* **2018**, *140* (5), 1743−1752.
(39) Bukola, S.; Beard, K.; Korzeniewski, C.; Harris, J. M.; Creager, S. E. Single-Layer Graphene Sandwiched between Proton-Exchange Membranes for Selective Proton Transmission. *ACS Appl. Nano Mater.* **2019**, *2* (2), 964−974.
(40) Lozada-Hidalgo, M.; Zhang, S.; Hu, S.; Esfandiar, A.; Grigorieva, I. v.; Geim, A. K. Scalable and Efficient Separation of Hydrogen Isotopes Using Graphene-Based Electrochemical Pumping. *Nature Comm* **2017**, *8* (1), 15215.
(41) Chen, Q.; Du, Y. Y.; Li, K. M.; Xiao, H. F.; Wang, W.; Zhang, W. M. Graphene Enhances the Proton Selectivity of Porous Membrane in Vanadium Flow Batteries. *Materials and Design* **2017**, *113*, 149−156.
(42) O'Hern, S. C.; Boutilier, M. S. H.; Idrobo, J. C.; Song, Y.; Kong, J.; Laoui, T.; Atieh, M.; Karnik, R. Selective Ionic Transport through Tunable Subnanometer Pores in Single-Layer Graphene Membranes. *Nano Lett.* **2014**, *14* (3), 1234−1241.
(43) Zhao, J.; He, G.; Huang, S.; Villalobos, L. F.; Dakhchoune, M.; Bassas, H.; Agrawal, K. v. Etching Gas-Sieving Nanopores in Single-Layer Graphene with an Angstrom Precision for High-Performance Gas Mixture Separation. *Sci. Adv.* **2019**, *5* (1), No. eaav1851.
(44) Qi, H.; Li, Z.; Tao, Y.; Zhao, W.; Lin, K.; Ni, Z.; Jin, C.; Zhang, Y.; Bi, K.; Chen, Y. Fabrication of Sub-Nanometer Pores on Graphene Membrane for Ion Selective Transport. *Nanoscale* **2018**, *10* (11), 5350−5357.
(45) Koenig, S. P.; Wang, L.; Pellegrino, J.; Bunch, J. S. Selective Molecular Sieving through Porous Graphene. *Nature Nanotechnol* **2012**, *7* (11), 728−732.
(46) Walker, M. I.; Ubych, K.; Saraswat, V.; Chalklen, E. A.; Braeuninger-Weimer, P.; Caneva, S.; Weatherup, R. S.; Hofmann, S.; Keyser, U. F. Extrinsic Cation Selectivity of 2D Membranes. *ACS Nano* **2017**, *11* (2), 1340−1346.
(47) Huang, S.; Dakhchoune, M.; Luo, W.; Oveisi, E.; He, G.; Rezaei, M.; Zhao, J.; Alexander, D. T. L.; Züttel, A.; Strano, M. S.; Agrawal, K. V. Single-Layer Graphene Membranes by Crack-Free Transfer for Gas Mixture Separation. *Nature Comm* **2018**, *9* (1), 1−11.
(48) Kim, S.; Choi, J.; Choi, C.; Heo, J.; Kim, D. W.; Lee, J. Y.; Hong, Y. T.; Jung, H. T.; Kim, H. T. Pore-Size-Tuned Graphene Oxide Frameworks as Ion-Selective and Protective Layers on Hydrocarbon Membranes for Vanadium Redox-Flow Batteries. *Nano Lett.* **2018**, *18* (6), 3962−3968.
(49) Kidambi, P. R.; Ducati, C.; Dlubak, B.; Gardiner, D.; Weatherup, R. S.; Martin, M.-B. B.; Seneor, P.; Coles, H.; Hofmann, S. The Parameter Space of Graphene Chemical Vapor Deposition on Polycrystalline Cu. *J. Phys. Chem. C* **2012**, *116* (42), 22492−22501.
(50) Kidambi, P. R.; Bayer, B. C.; Blume, R.; Wang, Z.-J.; Baehtz, C.; Weatherup, R. S.; Willinger, M.-G.; Schloegl, R.; Hofmann, S. Observing Graphene Grow: Catalyst−Graphene Interactions during Scalable Graphene Growth on Polycrystalline Copper. *Nano Lett.* **2013**, *13* (10), 4769−4778.
(51) Xu, X.; Zhang, Z.; Dong, J.; Yi, D.; Niu, J.; Wu, M.; Lin, L.; Yin, R.; Li, M.; Zhou, J.; Wang, S.; Sun, J.; Duan, X.; Gao, P.; Jiang, Y.; Wu, X.; Peng, H.; Ruoff, R. S.; Liu, Z.; Yu, D.; Wang, E.; Ding, F.; Liu, K. Ultrafast Epitaxial Growth of Metre-Sized Single-Crystal Graphene on Industrial Cu Foil. *Science Bulletin* **2017**, *62* (15), 1074−1080.
(52) Vlassiouk, I. v.; Stehle, Y.; Pudasaini, P. R.; Unocic, R. R.; Rack, P. D.; Baddorf, A. P.; Ivanov, I. N.; Lavrik, N. v.; List, F.; Gupta, N.; Bets, K. v.; Yakobson, B. I.; Smirnov, S. N. Evolutionary Selection Growth of Two-Dimensional Materials on Polycrystalline Substrates. *Nat. Mater.* **2018**, *17* (4), 318−322.
(53) Wu, T.; Zhang, X.; Yuan, Q.; Xue, J.; Lu, G.; Liu, Z.; Wang, H.; Wang, H.; Ding, F.; Yu, Q.; Xie, X.; Jiang, M. Fast Growth of Inch-Sized Single-Crystalline Graphene from a Controlled Single Nucleus on Cu−Ni Alloys. *Nat. Mater.* **2016**, *15* (1), 43−47.

https://doi.org/10.1021/acsnano.2c03730
ACS Nano 2022, 16, 16003−16018

(54) Villalobos, L. F.; van Goethem, C.; Hsu, K.-J.; Li, S.; Moradi, M.; Zhao, K.; Dakhchoune, M.; Huang, S.; Shen, Y.; Oveisi, E.; Boureau, V.; Agrawal, K. V. Bottom-up Synthesis of Graphene Films Hosting Atom-Thick Molecular-Sieving Apertures. *Proc. Natl. Acad. Sci. U.S.A.* **2021**, *118* (37), e2022201118.
(55) Zhao, T.; Xu, C.; Ma, W.; Liu, Z.; Zhou, T.; Liu, Z.; Feng, S.; Zhu, M.; Kang, N.; Sun, D.-M.; Cheng, H.-M.; Ren, W. Ultrafast Growth of Nanocrystalline Graphene Films by Quenching and Grain-Size-Dependent Strength and Bandgap Opening. *Nat. Commun.* **2019**, *10* (1), 4854.
(56) Toh, C. T.; Zhang, H.; Lin, J.; Mayorov, A. S.; Wang, Y. P.; Orofeo, C. M.; Ferry, D. B.; Andersen, H.; Kakenov, N.; Guo, Z.; Abidi, I. H.; Sims, H.; Suenaga, K.; Pantelides, S. T.; Özyilmaz, B. Synthesis and Properties of Free-Standing Monolayer Amorphous Carbon. *Nature* **2020**, *577* (7789), 199−203.
(57) Zeng, Z.; Song, R.; Zhang, S.; Han, X.; Zhu, Z.; Chen, X.; Wang, L. Biomimetic N-Doped Graphene Membrane for Proton Exchange Membranes. *Nano Lett.* **2021**, *21* (10), 4314.
(58) Dong, J.; Zhang, L.; Ding, F. Kinetics of Graphene and 2D Materials Growth. *Adv. Mater.* **2019**, *31* (9), 1801583.
(59) Vlassiouk, I.; Regmi, M.; Fulvio, P.; Dai, S.; Datskos, P.; Eres, G.; Smirnov, S. Role of Hydrogen in Chemical Vapor Deposition Growth of Large Single-Crystal Graphene. *ACS Nano* **2011**, *5* (7), 6069−6076.
(60) Chaitoglou, S.; Bertran, E. Effect of Temperature on Graphene Grown by Chemical Vapor Deposition. *J. Mater. Sci.* **2017**, *52* (13), 8348−8356.
(61) Zhang, Z.; Lagally, M. G. Atomistic Processes in the Early Stages of Thin-Film Growth. *Science* **1997**, *276* (5311), 377−383.
(62) Vlassiouk, I.; Smirnov, S.; Regmi, M.; Surwade, S. P.; Srivastava, N.; Feenstra, R.; Eres, G.; Parish, C.; Lavrik, N.; Datskos, P.; Dai, S.; Fulvio, P. Graphene Nucleation Density on Copper: Fundamental Role of Background Pressure. *J. Phys. Chem. C* **2013**, *117* (37), 18919−18926.
(63) Kim, H.; Mattevi, C.; Calvo, M. R.; Oberg, J. C.; Artiglia, L.; Agnoli, S.; Hirjibehedin, C. F.; Chhowalla, M.; Saiz, E. Activation Energy Paths for Graphene Nucleation and Growth on Cu. *ACS Nano* **2012**, *6* (4), 3614−3623.
(64) Zhang, Y.; Li, Z.; Kim, P.; Zhang, L.; Zhou, C. Anisotropic Hydrogen Etching of Chemical Vapor Deposited Graphene. *ACS Nano* **2012**, *6* (1), 126−132.
(65) Choubak, S.; Biron, M.; Levesque, P. L.; Martel, R.; Desjardins, P. No Graphene Etching in Purified Hydrogen. *J. Phys. Chem. Lett.* **2013**, *4* (7), 1100−1103.
(66) Jacobberger, R. M.; Arnold, M. S. Graphene Growth Dynamics on Epitaxial Copper Thin Films. *Chem. Mater.* **2013**, *25* (6), 871−877.
(67) Ma, T.; Ren, W.; Zhang, X.; Liu, Z.; Gao, Y.; Yin, L. C.; Ma, X. L.; Ding, F.; Cheng, H. M. Edge-Controlled Growth and Kinetics of Single-Crystal Graphene Domains by Chemical Vapor Deposition. *Proc. Natl. Acad. Sci. U. S. A.* **2013**, *110* (51), 20386−20391.
(68) Li, X.; Magnuson, C. W.; Venugopal, A.; Tromp, R. M.; Hannon, J. B.; Vogel, E. M.; Colombo, L.; Ruoff, R. S. Large-Area Graphene Single Crystals Grown by Low-Pressure Chemical Vapor Deposition of Methane on Copper. *J. Am. Chem. Soc.* **2011**, *133* (9), 2816−2819.
(69) Jia, C.; Jiang, J.; Gan, L.; Guo, X. Direct Optical Characterization of Graphene Growth and Domains on Growth Substrates. *Sci. Rep.* **2012**, *2* (1), 707.
(70) Ferrari, A. C. Raman Spectroscopy of Graphene and Graphite: Disorder, Electron-Phonon Coupling, Doping and Nonadiabatic Effects. *Solid State Commun.* **2007**, *143* (1−2), 47−57.
(71) Ugeda, M. M.; Fernández-Torre, D.; Brihuega, I.; Pou, P.; Martínez-Galera, A. J.; Pérez, R.; Gómez-Rodríguez, J. M. Point Defects on Graphene on Metals. *Phys. Rev. Lett.* **2011**, *107* (11), 116803.
(72) Jung, S. H.; Seo, Y. M.; Gu, T.; Jang, W.; Kang, S. G.; Hyeon, Y.; Hyun, S. H.; Lee, J. H.; Whang, D. Super-Nernstian PH Sensor Based on Anomalous Charge Transfer Doping of Defect-Engineered Graphene. *Nano Lett.* **2021**, *21* (1), 34−42.
(73) Shreiner, R. H.; Pratt, K. W.*Standard Reference Materials: Primary Standards and Standard Reference Materials for Electrolytic Conductivity*; NIST Special Publication 260-142, 2004 Ed.; National Institute of Standards and Technology: Gaithersburg, MD, 2004.
(74) Yeager, H. L.; O'Dell, B.; Twardowski, Z. Transport Properties of Nafion® Membranes in Concentrated Solution Environments. *J. Electrochem. Soc.* **1982**, *129* (1), 85−89.
(75) Geise, G. M.; Freeman, B. D.; Paul, D. R. Sodium Chloride Diffusion in Sulfonated Polymers for Membrane Applications. *J. Membr. Sci.* **2013**, *427*, 186−196.
(76) Lehmani, A.; Turq, P.; Périé, M.; Périé, J.; Simonin, J. P. Ion Transport in Nafion® 117 Membrane. *J. Electroanal. Chem.* **1997**, *428* (1−2), 81−89.
(77) Hsu, W. Y.; Gierke, T. D. Ion Transport and Clustering in Nafion Perfluorinated Membranes. *J. Membr. Sci.* **1983**, *13* (3), 307−326.
(78) Boutilier, M. S. H. H.; Sun, C.; O'Hern, S. C.; Au, H.; Hadjiconstantinou, N. G.; Karnik, R. Implications of Permeation through Intrinsic Defects in Graphene on the Design of Defect-Tolerant Membranes for Gas Separation. *ACS Nano* **2014**, *8* (1), 841−849.
(79) Mi, B. Scaling up Nanoporous Graphene Membranes. *Science* **2019**, *364* (6445), 1033−1034.
(80) Ying, Z.; Gao, Y.; Meng, Y.; Cheng, Y.; Shi, L. Influence of Stacking on the Aqueous Proton Penetration Behaviour across Two-Dimensional Graphtetrayne. *Nanoscale* **2021**, *13* (11), 5757−5764.
(81) Hu, S.; Gopinadhan, K.; Rakowski, A.; Neek-Amal, M.; Heine, T.; Grigorieva, I. v.; Haigh, S. J.; Peeters, F. M.; Geim, A. K.; Lozada-Hidalgo, M. Transport of Hydrogen Isotopes through Interlayer Spacing in van Der Waals Crystals. *Nat. Nanotechnol.* **2018**, *13* (6), 468−472.
(82) Zakertabrizi, M.; Hosseini, E.; Habibnejad Korayem, A.; Razmjou, A. Hydrous Proton Transfer through Graphene Interlayer: An Extraordinary Mechanism under Magnifier. *Adv. Mater. Technol.* **2021**, *6* (10), 2001049.
(83) Mouterde, T.; Keerthi, A.; Poggioli, A. R.; Dar, S. A.; Siria, A.; Geim, A. K.; Bocquet, L.; Radha, B. Molecular Streaming and Its Voltage Control in Ångström-Scale Channels. *Nature* **2019**, *567* (7746), 87−90.
(84) Suk, M. E.; Aluru, N. R. Ion Transport in Sub-5-Nm Graphene Nanopores. *J. Chem. Phys.* **2014**, *140* (8), 084707.
(85) O'hern, S. C.; Stewart, C. A.; Boutilier, M. S. H.; Idrobo, J.-C.; Bhaviripudi, S.; Das, S. K.; Kong, J.; Laoui, T.; Atieh, M.; Karnik, R. Selective Molecular Transport through Intrinsic Defects in a Single Layer of CVD Graphene. *ACS Nano* **2012**, *6* (11), 10130−10138.
(86) Rollings, R. C.; Kuan, A. T.; Golovchenko, J. A. Ion Selectivity of Graphene Nanopores. *Nat. Commun.* **2016**, *7* (1), 1−7.
(87) Wang, R.; Zhang, W.; He, G.; Gao, P. Controlling Fuel Crossover and Hydration in Ultra-Thin Proton Exchange Membrane-Based Fuel Cells Using Pt-Nanosheet Catalysts. *J. Mater. Chem. A* **2014**, *2* (39), 16416−16423.
(88) Sayadi, P.; Rowshanzamir, S.; Parnian, M. J. Study of Hydrogen Crossover and Proton Conductivity of Self-Humidifying Nanocomposite Proton Exchange Membrane Based on Sulfonated Poly (Ether Ether Ketone). *Energy* **2016**, *94*, 292−303.
(89) Guccini, V.; Carlson, A.; Yu, S.; Lindbergh, G.; Lindström, R. W.; Salazar-Alvarez, G. Highly Proton Conductive Membranes Based on Carboxylated Cellulose Nanofibres and Their Performance in Proton Exchange Membrane Fuel Cells. *J. Mater. Chem. A* **2019**, *7* (43), 25032−25039.
(90) Chaturvedi, P.; Moehring, N. K.; Cheng, P.; Vlassiouk, I.; Boutilier, M. S. H.; Kidambi, P. R. Deconstructing Proton Transport Through Atomically Thin Monolayer CVD Graphene Membranes. *J. Mater. Chem. A* **2022**, DOI: 10.1039/D2TA01737G.